Hadronic photon-photon interactions at high energies

R. Engel
Institut für Theoretische Physik, Universität Leipzig, D-04109 Leipzig, Germany
and Universität Siegen, Fachbereich Physik, D-57068 Siegen, Germany

J. Ranft*
Laboratoire de Physique des Particules, Institut National de Physique Nucléaire et de Physique des Particules, Boîte Postale 110, F-74941 Annecy-le-Vieux, France

(Received 21 September 1995; revised manuscript received 23 May 1996)

Photon-photon collisions are investigated in the framework of the two-component dual parton model. The model contains contributions from direct, resolved soft, and resolved hard interactions. All free parameters of the model are determined in fits to hadron-hadron and photon-hadron cross section data. The model is shown to agree well with hadron production data from hadron-hadron and photon-hadron collisions. The multiparticle production in hadron-hadron, photon-hadron, and photon-photon collisions as predicted by the model is compared. Strong differences are only found as a function of the transverse momentum variable. The hadron production in photon-photon collisions at present and future electron-positron colliders is studied using photon spectra according to bremsstrahlung, beamstrahlung, and backscattered laser radiation. [S0556-2821(96)01319-7]

PACS number(s): 12.40.Nn, 13.60.−r, 13.65.+i

I. INTRODUCTION

The photon, in its high-energy interactions with hadrons, behaves very much like a hadron, however, with cross sections reduced strongly against purely hadronic cross sections. In addition to this soft hadronic interaction, usually described using the vector dominance model (VDM), the photon has a direct (QED) pointlike interaction with the hadronic constituents and it has a resolved hard interaction between its hadronic constituents and the hadronic constituents of the target. At moderate energies these hard interactions of the photons do not change significantly some of the minimum bias properties of photon-hadron and photon-photon interactions, such as, for example, the average multiplicities or pseudorapidity distributions. This is often forgotten if only the hard part of the photon interaction is discussed. Of course, these hard interactions dominate transverse momentum distributions of produced hadrons and jets. Even at high energies, hadronic interactions of photons are characterized by soft multiparticle production. Since the soft component of hadron production cannot be understood purely on the basis of perturbative QCD, one has to rely on models to calculate the multiparticle final states. The dual parton model (DPM) (a recent review is given in Ref. [1]) has been very successfully describing soft hadronic processes in hadron-hadron collisions. Observations such as rapidity plateaus and average transverse momenta rising with energy, Koba-Nielsen-Olesen (KNO) scaling violation, transverse momentum-multiplicity correlations, and minijets pointed out that soft and hard processes are closely related. These properties were understood within the two-component dual parton model for hadron-hadron interactions by Aurenche *et al.* [2–8].

Assuming a universal behavior of soft hadronic interactions, it is possible to extend the dual parton model to hadronic interactions involving photons. The first studies of photon-hadron interactions in the framework of the two-component dual parton model were done by Engel [9–11]. This reaction was studied within other models by various authors; one example is the work by Schuler and Sjöstrand [12,13] which is also available within the event generator PYTHIA [14].

Here we apply the model described in [9,11] to the study of hadronic photon-photon interactions. In Sec. II we give a brief introduction to the dual parton model used to describe photon-hadron and photon-photon collisions; a complete account of the model can be found in [9,11]. An overview of the model realization in the Monte Carlo event generator PHOJET is given. We study with PHOJET hadron-hadron and photon-hadron collisions and compare to data in Sec. III. In Sec. IV we compare the properties of minimum-bias hadron production as calculated with PHOJET in hadron-hadron, photon-hadron, and photon-photon collisions. In Sec. V we discuss the properties of hadron production via photon-photon collisions at present and future electron-positron colliders. A summary is given in Sec. VI.

II. EVENT GENERATOR PHOJET

The realization of the dual parton model with a hard and a soft component in PHOJET is similar to the event generator DTUJET-93 [2,8] simulating p-p and p-$\bar{p}$ collisions up to very high energies. In the following, we restrict our discussion of the model to the basic ideas rather than giving the complete expressions for all the formulas and quantities entering the model. More detailed descriptions of the model are given in [9,11].

In the model, the dual nature of the photon is taken into account by considering the physical photon state as a super-

*Present address: Departamento Física de Partículas, Universidade de Santiago de Compostela, Spain.

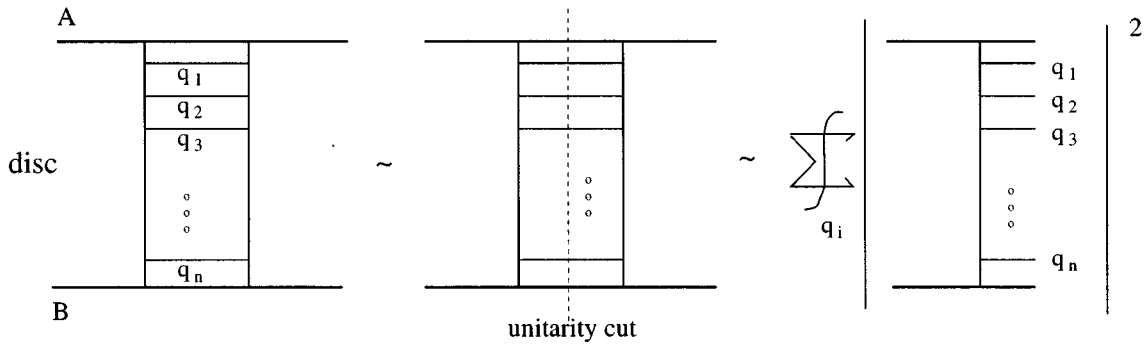

FIG. 1. Graphical presentation of the optical theorem: the discontinuity of the elastic scattering amplitude at vanishing momentum transfer can be considered a unitarity cut through all intermediate particle propagators, restricting these particles to the mass shell. Besides trivial kinematical factors, the discontinuity corresponds to the total cross section.

position of a ''bare photon'' and virtual hadronic states having the same quantum numbers $J^{PC}=1^{--}$ as the photon. Since the properties of the high-mass hadronic fluctuations of the photon are not well known, it is necessary to introduce some approximations for calculations. To keep the model as simple as possible, two generic hadronic states $|q\overline{q}\rangle$ and $|q\overline{q^{\star}}\rangle$ have been introduced to describe the hadronic piece of the photon. The low-mass state $|q\overline{q}\rangle$ corresponds to the superposition of the vector mesons ρ, ω, and ϕ and a $\pi^{+}\pi^{-}$ background. The state $|q\overline{q^{\star}}\rangle$ is used as an approximation for hadronic states with higher masses (e.g., ρ', ω', or ρ''). The physical photon reads

$$|\gamma\rangle=\sqrt{Z_3}|\gamma_{\rm bare}\rangle+|\gamma_{\rm had}\rangle, \tag{1}$$

with

$$Z_3=1-\frac{e^2}{f^2_{q\overline{q}}}-\frac{e^2}{f^2_{q\overline{q^{\star}}}} \quad \text{and} \quad |\gamma_{\rm had}\rangle=\frac{e}{f_{q\overline{q}}}|q\overline{q}\rangle+\frac{e}{f_{q\overline{q^{\star}}}}|q\overline{q^{\star}}\rangle, \tag{2}$$

where e denotes the elementary charge.

The interactions of the hadronic fluctuations are described within the dual parton model in terms of Reggeon ($\mathbb{R}$) and Pomeron ($\mathbb{P}$) exchanges. For soft processes, photon-hadron duality is used. The energy dependence of the Reggeon and Pomeron amplitude is assumed to be the same for all hadronic processes. Therefore, data on hadron-hadron and photon-hadron cross sections can be used to determine the parameters necessary to describe soft photon-photon interactions. However, one does not expect that this photon-hadron universality holds for processes involving short distances (high transverse momenta). There, long- and short-living fluctuations can contribute.

In the following we assume that hadronic interactions at high energies can be described by the exchange of a single generic Pomeron. This Pomeron exchange is taken to correspond to graphs with multiperipheral kinematics [15]. The total Pomeron cross section can be calculated from the discontinuity of the elastic scattering amplitude. The optical theorem relates the discontinuity of the Pomeron amplitude to diagrams with all possible final states (see Fig. 1). In order to get the cross section corresponding to such diagrams one has to sum and integrate over these states as intermediate particles with the momenta q_i. In general, the calculation of the cross section is not possible within perturbative QCD. However, the integration over the transverse momenta of the intermediate states can be split into two parts, the integration over momenta with $p_\perp<p_\perp^{\rm cutoff}$ and the integration over momenta with $p_\perp\geqslant p_\perp^{\rm cutoff}$. The graphs are artificially subdivided into two classes; the first describes only *soft* processes and the second sums all the other graphs with at least one large momentum transfer (*hard* processes). For simplicity, all intermediate states are assumed to be partons. Soft and hard processes are distinguished by applying the transverse momentum cutoff $p_\perp^{\rm cutoff}$ to these partons.

In the model, the cross section of hard processes is estimated using the framework of the QCD-improved parton model with lowest-order matrix elements [16,17]. Assuming a purely imaginary Pomeron amplitude, the optical theorem is used to relate the cross section of the hard processes to the hard part of the Pomeron amplitude. For example, the contribution $A_{2g}^{\rm ela}$ of the simplest nontrivial Pomeron graph with two high-$p_\perp$ ''ladder'' gluons having the momenta q_1 and q_2 is given by

$$A_{2g}^{\rm ela}=i\,{\rm disc}(A_{2g}^{\rm ela})=is\sigma^{\rm parton\ model}_{AB\to ggX}, \tag{3}$$

where s is the squared center-of-mass system (c.m.s.) energy.

The cross section corresponding to the graphs describing soft processes only is parametrized using Regge arguments by a supercritical Pomeron pole. Of course, the parameters entering the expression for the soft cross section depend on the value of the cutoff to distinguish between soft and hard processes.

On the Born-graph level, for example, the photon-photon cross sections read as follows.

(i) The Reggeon and Pomeron exchange (soft processes only)

$$\sigma_{\mathbb{P}}^{\rm tot}(s)=\left(\frac{e^2}{f^2_{q\overline{q}}}\right)^2 g_{\mathbb{P},q\overline{q}}(0)g_{\mathbb{P},q\overline{q}}(0)\left(\frac{s}{s_0}\right)^{\Delta_{\mathbb{P}}},$$

$$\sigma_{\mathbb{R}}^{\rm tot}(s)=\left(\frac{e^2}{f^2_{q\overline{q}}}\right)^2 g_{\mathbb{R},q\overline{q}}(0)g_{\mathbb{R},q\overline{q}}(0)\left(\frac{s}{s_0}\right)^{\Delta_{\mathbb{R}}}, \tag{4}$$

with $\Delta_{\mathbb{P}}=\alpha_{\mathbb{P}}(0)-1$ and $\Delta_{\mathbb{R}}=\alpha_{\mathbb{R}}(0)-1$. Here we denote with $\alpha_{\mathbb{P}}(0)$ [$\alpha_{\mathbb{R}}(0)$] the Pomeron [Reggeon] intercept, and

with $g_{\mathbb{P},q\bar{q}}$ ($g_{\mathbb{R},q\bar{q}}$) the couplings of the Pomeron (Reggeon) to the hadronic qq fluctuations.

(ii) The hard double-resolved photon-photon interaction

$$\sigma_{\text{d-res}}^{\text{hard}}(s,p_\perp^{\text{cutoff}}) = \int dx_1 dx_2 d\hat{t} \sum_{i,j,k,l} \frac{1}{1+\delta_{k,l}} f_{\gamma,i}(x_1,Q^2) f_{\gamma,j}(x_2,Q^2) \times \frac{d\sigma_{i,j\to k,l}^{\text{QCD}}(\hat{s},\hat{t})}{d\hat{t}} \Theta(p_\perp - p_\perp^{\text{cutoff}}), \quad (5)$$

where $f_{\gamma,i}(x_1,Q^2)$ is the distribution of the parton i in the photon and the sum includes all possible parton configurations i,j,k,l.

(iii) The single-resolved interaction

$$\sigma_{\text{s-res}}(s,p_\perp^{\text{cutoff}}) = \int dx d\hat{t} \sum_{i,k,l} f_{\gamma,i}(x,Q^2) \frac{d\sigma_{\gamma,i\to k,l}^{\text{QCD}}(\hat{s},\hat{t})}{d\hat{t}} \times \Theta(p_\perp - p_\perp^{\text{cutoff}}). \quad (6)$$

(iv) The direct interaction

$$\sigma_{\text{dir}}(s,p_\perp^{\text{cutoff}}) = \int d\hat{t} \sum_k \frac{d\sigma_{\gamma,\gamma\to k,\bar{k}}(\hat{s},\hat{t})}{d\hat{t}} \Theta(p_\perp - p_\perp^{\text{cutoff}}). \quad (7)$$

For simplicity, we have written the cross section formulas only for the low-mass state $|q\bar{q}\rangle$. Similar expressions are used for interactions involving the $|q\bar{q}^*\rangle$ state. If not explicitly stated, all the calculations have been done using the leading-order Gluck-Reya-Vogt (GRV) parton distribution functions for the proton [18] and the photon [19].

Assuming Gaussian distributions in impact parameter space, the amplitudes for the different processes can be calculated from the cross sections given above.

The amplitudes corresponding to the one-Pomeron exchange between the hadronic fluctuations are unitarized applying a two-channel eikonal formalism similar to [20,2]. Note that only the double-resolved contributions to the Born-graph amplitude (double-resolved soft and hard scatterings) are eikonalized [21–23]. The unitarity corrections to single-resolved and direct interactions are suppressed by additional powers of the fine structure constant α_{em} and can be neglected. In impact parameter representation, the eikonalized scattering amplitude for resolved photon interactions has the structure

$$a_{\text{res}}(s,B) = \frac{i}{2}\left(\frac{e^2}{f_{q\bar{q}}^2}\right)^2 (1-e^{-\chi(s,B)}), \quad (8)$$

with the eikonal function

$$\chi(s,B) = \chi_S(s,B) + \chi_H(s,B) + \chi_D(s,B) + \chi_C(s,B). \quad (9)$$

Here, $\chi_i(s,B)$ denotes the contributions from the different Born graphs: (S) the soft part of the Pomeron and Reggeon, (H) the hard part of the Pomeron, (D) the triple- and loop-Pomeron, and (C) the double-Pomeron graphs. To get the photon-photon scattering amplitude, the resolved and the direct amplitudes given by perturbative QCD are summed up. The complete expressions will be given in [11].

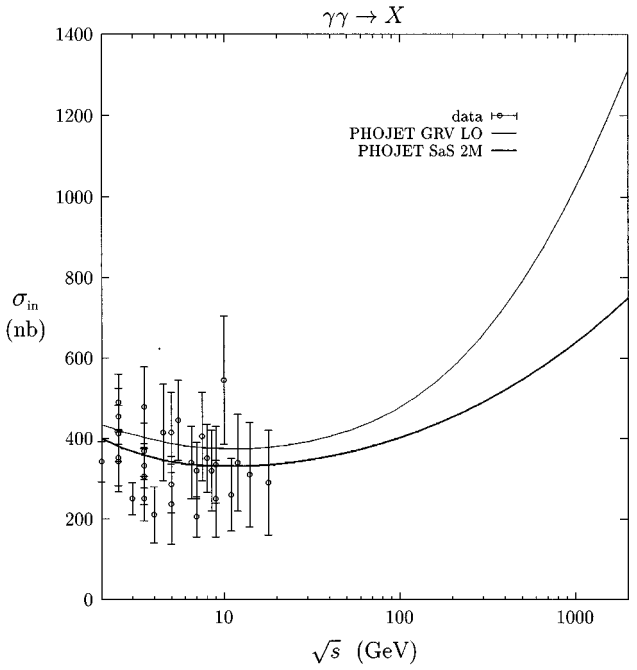

FIG. 2. Inelastic photon-photon cross sections as calculated in the model compared with experimental data at low energies [57,70–73]. The two curves from the model were calculated using the GRV LO photon structure function [19] and the SaS 2M photon structure function [51]. The differences between both curves at high energy demonstrate the uncertainties of the predictions due to the limited data available on the photon structure function. Our curve calculated with the SaS 2M structure function agrees practically with the cross section calculated with the same structure function but using another model by Schuler and Sjöstrand [13].

The probabilities to find a photon in one of the generic hadronic states, the coupling constants to the Reggeon and Pomeron, and the effective Reggeon and Pomeron intercepts cannot be determined by basic principles. These quantities are treated as free parameters. It was shown in [9] that it is possible to fix the free parameters by a global fit to proton-proton and photon-proton cross sections and elastic slope parameters. In Fig. 2 we show the model predictions for the inelastic photon-photon cross section (including quasielastic vector meson production). The diffractive cross sections of quasielastic vector meson production ($V=\rho$, ω, and ϕ), single-diffraction dissociation, and double-diffraction dissociation are given in Fig. 3. In order to show the strong dependence of the model extrapolations on the parton densities of the photon, the cross sections have been calculated with two different parametrizations of the parton distribution functions.

Once the free parameters are determined, the probabilities for the different final state configurations are calculated from the discontinuity of the elastic photon-photon scattering amplitude (optical theorem). The total discontinuity can be expressed as a sum of graphs with k_c soft Pomeron cuts, l_c hard Pomeron cuts, m_c triple- or loop-Pomeron cuts, and n_c double-Pomeron cuts by applying the Abramovski-Gribov-Kancheli (AGK) cutting rules [24,25]. In impact parameter space one gets, for the inelastic cross section,

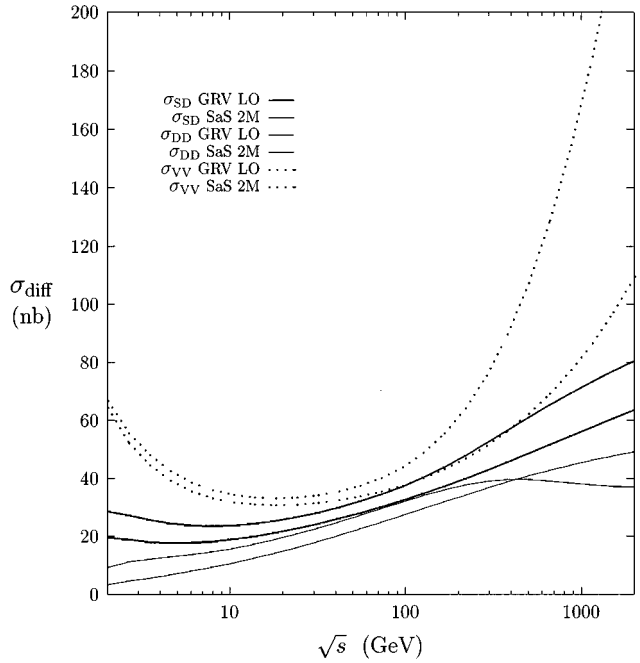

FIG. 3. Diffractive cross sections as calculated with PHOJET using the GRV LO photon structure function [19] and the SaS 2M photon structure function [51]. The upper curve is for each of the three cross sections, the one obtained with the GRV LO structure function.

$$\sigma(k_c,l_c,m_c,n_c,s,B)=\frac{(2\chi_S)^{k_c}}{k_c!}\frac{(2\chi_H)^{l_c}}{l_c!}\frac{(2\chi_D)^{m_c}}{m_c!}\frac{(2\chi_C)^{n_c}}{n_c!}\times\exp[-2\chi(s,B)], \tag{10}$$

with

$$\int d^2B \sum_{k_c+l_c+m_c+n_c=1}^{\infty}\sigma(k_c,l_c,m_c,n_c,s,B)\approx\sigma_{\rm tot}-\sigma_{\rm qel}, \tag{11}$$

where $\sigma_{\rm tot}$ and $\sigma_{\rm qel}$ denote the total cross section and the cross section of quasielastic vector meson production, respectively. We use here the conventions of [9] treating the triple- and loop-Pomeron cross sections (and hence χ_D) as negative quantities. In [2] the negative sign is explicitly written in the cross section formulas (10). These negative cross sections are not directly related to physical processes. For example, the triple-Pomeron graph represents an absorptive correction; it has to be summed with the single-Pomeron exchange graph, reducing the total cross section. Since the triple-Pomeron graph involves three Pomerons, one has to apply the AGK cutting rules to calculate the contribution of this graph to physical processes. For example, the diffractive cut of this graph (corresponding to the well-known description of diffraction by Pomeron-particle scattering) has the AGK weight of -1. Together with the negative sign of the triple-Pomeron cross section, this gives a positive, experimentally observable cross section for diffraction. In general, for all graphs involving more than one Pomeron, a resummation according to the AGK cutting rules is done [2,11] to allow for the probability interpretation of Eq. (10).

The influence of a weak photon virtuality P^2 on the total cross section is estimated using arguments of the generalized VDM (GVDM). For definiteness let us consider the photon-photon cross section at e^+e^- colliders. The total cross section can be divided into partial cross sections according to the photon polarizations [T (S) for transverse (scalar) photons; see Refs. [26,27]]

$$\sigma_{\gamma\gamma}^{\rm tot,\ expt}(P_1^2,P_2^2,s)=\sigma_{TT}^{\rm tot}(P_1^2,P_2^2,s)+\epsilon_1\sigma_{ST}^{\rm tot}(P_1^2,P_2^2,s)+\epsilon_2\sigma_{TS}^{\rm tot}(P_1^2,P_2^2,s)+\epsilon_1\epsilon_2\sigma_{SS}^{\rm tot}(P_1^2,P_2^2,s). \tag{12}$$

The polarization parameters ϵ_i depend on the electron beams creating the photon flux. For unpolarized electron beams the values of ϵ_i were found to be close to 1 (see, for example, [28]). In the following we use the approximation suggested in [27], setting $\epsilon_1=\epsilon_2=1$. The experimental cross section is parametrized by [27]

$$\sigma_{\gamma\gamma}^{\rm tot,\ expt}(P_1^2,P_2^2,s)=\sigma_{\gamma\gamma}^{\rm tot}(0,0,s)F(P_1^2)F(P_2^2), \tag{13}$$

with

$$F(P^2)=\sum_{V=\rho,\omega,\phi} r_V\frac{1+P^2/(4m_V^2)}{(1+P^2/m_V^2)^2}+r_{\rm eff}\frac{1}{1+P^2/m_{\rm eff}^2},\qquad F(0)=1. \tag{14}$$

The influence of high-mass vector mesons and continuum contributions is taken into account by the last term of the sum. The parameters occurring in Eq. (14) are given in [27]. The suppression of the parton content of the photon due to the photon virtuality P^2 is approximated by the parametrizations [29–31]

$$f_{\gamma,q_i}(x,Q^2,P^2)=f_{\gamma,q_i}(x,Q^2)\frac{\ln[Q^2/(P^2+m_\rho^2)]}{\ln(Q^2/m_\rho^2)}, \tag{15}$$

$$f_{\gamma,g}(x,Q^2,P^2)=f_{\gamma,g}(x,Q^2)\frac{\ln^2[Q^2/(P^2+m_\rho^2)]}{\ln^2(Q^2/m_\rho^2)}. \tag{16}$$

Events with n soft Pomeron cuts ($n\geqslant 2$, multiple interaction) are suppressed with a factor

$$P_{\rm sup}=\left(\frac{m_{\rm sup}^2}{(P_1^2+m_{\rm sup}^2)}\frac{m_{\rm sup}^2}{(P_2^2+m_{\rm sup}^2)}\right)^{n-1}, \tag{17}$$

where the effective mass $m_{\rm sup}$ is assumed to be the ρ mass.

In the Monte Carlo realization of the model, the different final state configurations are sampled from Eq. (10). For Pomeron cuts involving a hard scattering, the complete parton kinematics and flavors or colors are sampled according to the parton model using the method of [32], extended to direct processes. In the model, initial state parton showers are generated using a backwards evolution algorithm similar to [33,34] with the parton virtuality as an evolution variable. For interacting photons, the direct splitting $\gamma\to q\bar{q}$ is approximately taken into account. During the parton shower generation, the probability to have a direct photon splitting is calculated comparing the anomalous contribution [35]

$$q(x,Q^2)=\frac{3\alpha_{\rm em}}{2\pi}e_q^2\left[[x^2+(1-x)^2]\ln\left(\frac{1-x}{x}\frac{Q^2}{m_q^2}\right)+8x(1-x)-1\right] \quad (18)$$

to the full photon parton distribution function (PDF). The quark mass m_q in Eq. (18) depends on the parametrization of the photon PDF and is set fitting the PDF at large x and Q^2. Final state parton showers are generated using the algorithm provided in the Lund Monte Carlo JETSET [14].

For Pomeron cuts without large momentum transfer, the partonic interpretation of the dual parton model is used: Photons or mesons are split into a quark-antiquark pair whereas baryons are approximated by a quark-diquark pair. The longitudinal momentum fractions of the partons are given by Regge asymptotics [36–39]. One obtains, for the valence quark (x) and diquark $(1-x)$ distribution in the proton,

$$\rho(x)\sim\frac{1}{\sqrt{x}}(1-x)^{1.5} \quad (19)$$

and, for the quark-antiquark distribution in the photon,

$$\rho(x)\sim\frac{1}{\sqrt{x(1-x)}}. \quad (20)$$

For multiple interaction events, the sea quark momenta are sampled from a

$$\rho(x)\sim\frac{1}{x} \quad (21)$$

distribution. Note that as a result of energy-momentum conservation, this distribution is influenced by the x distributions of the valence partons and asymmetric multiple interaction effects (for example, in photon-proton scattering). This will be discussed in detail elsewhere [11]. The transverse momenta of the soft partons are sampled from the distribution

$$\frac{d^2N_s}{d^2p_\perp}\sim\exp(-\beta p_\perp). \quad (22)$$

The energy-dependent slope parameter β is calculated from the requirement to have a smooth transition between the transverse momentum distributions of the soft constituents and the hard scattered partons.

For diffraction dissociation or double-Pomeron scattering, the parton configurations are generated using the same ideas described above applied to Pomeron-photon, hadron, or Pomeron scattering processes. Hence, a diffractive triple- or loop-Pomeron cut can involve hard scattering subprocesses, resulting in a rapidity gap event with jets. According to the kinematics of the triple- or loop-Pomeron graphs, the mass of the diffractively dissociating systems is sampled from a $1/M_D^{2\alpha_{\rm I\!P}(0)}$ distribution. The momentum transfer in diffraction is obtained from an exponential distribution with mass-dependent slope (see Ref. [9]). For the parton distributions of the Pomeron, the Capella–Kaidalov–Merino–Tran Thanh Van (CKMT) parametrization with a hard gluonic component [40,41] is used.

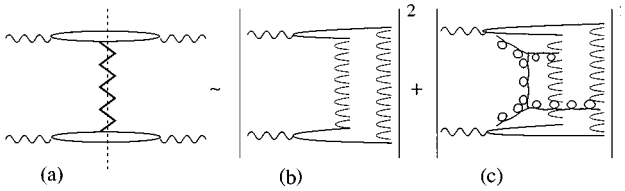

FIG. 4. Unitarity cut of a one-Pomeron graph: the unitarity sum including all possible final states is subdivided into final states with low-$p_\perp$ partons and into final states with at least one parton satisfying $p_\perp \geqslant p_\perp^{\rm cutoff}$.

Finally, the fragmentation of the sampled partonic final states is done by forming color neutral strings between the partons according to the color flow. For soft processes, the color flow is approximated using the expansion of QCD for large numbers of colors and flavors. This leads to a two-chain configuration characterizing a cut Pomeron [as shown in Figs. 4(a) and 4(b)] and a one-chain system for a cut Reggeon. In hard interactions the color flow is taken from the matrix elements directly [42]. The leading contributions of the matrix elements give a two-chain structure which corresponds to a cut Pomeron. For example, a cut of a single hard Pomeron graph (hard gluon-gluon scattering) is shown in Fig. 4(c). This method is also applied to the direct photon interactions.

The chains are fragmented using the fragmentation code JETSET 7.3 [14].

Note that due to this construction, the model predictions have only a weak dependence on the transverse momentum cutoff chosen to distinguish between soft and hard interactions. Decreasing the value of the cutoff leads to an increase

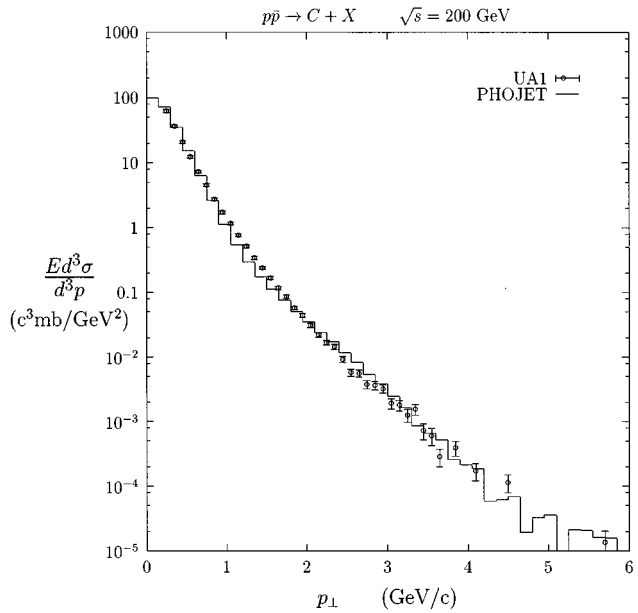

FIG. 5. Comparison of transverse momentum distributions of charged hadrons with collider data at $\sqrt{s}=200$ GeV [44]. The calculation uses the dual parton model code PHOJET.

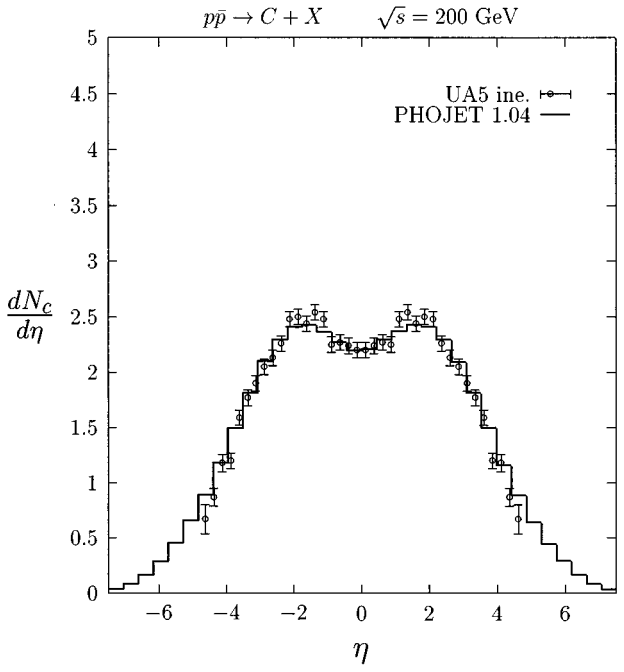

FIG. 6. Pseudorapidity distributions of charged hadrons produced in $\overline{p}$-p collisions as calculated with PHOJET are compared to collider data from the UA-5 Collaboration [45] for the energy $\sqrt{s}=200$ GeV.

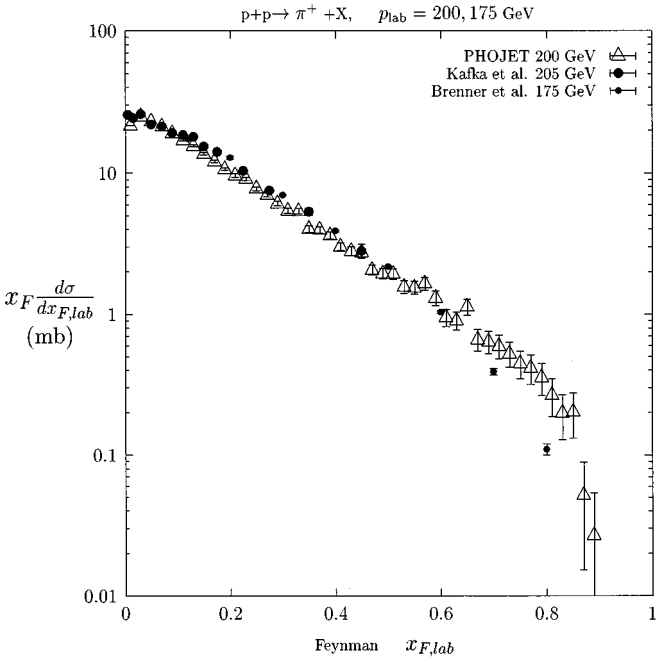

FIG. 7. Comparison of Feynman x_F distributions of π^+ mesons produced in proton-proton collisions at 205 and 175 GeV. The experimental data are from Kafka *et al.* [74] and from Brenner *et al.* [75]. The data from both experiments agree rather well with each other. The calculation uses the dual parton model PHOJET.

of the interactions which are classified as hard scatterings. However, since the soft parameters are fitted to the experimentally measured cross sections, the coupling constants of the soft part of the Pomeron depend also on the transverse momentum cutoff, compensating the increase of the hard part of the Pomeron. This results in an almost cutoff-independent Born cross section of the Pomeron. Finally, the constraint to have a smooth transition in the transverse momentum distributions of the soft and hard partons removes the ambiguity introduced in the model by the transverse momentum cutoff.

III. HADRON-HADRON AND PHOTON-HADRON COLLISIONS WITH PHOJET

Hadron production in hadron-hadron collisions has been extensively studied within the two-component dual parton model using the DTUJET model [2,8] in p-p and $\overline{p}$-p collisions and using the DPMJET-II model [43] in hadron-hadron, hadron-nucleus, and nucleus-nucleus collisions. Hadron production in photon-hadron collisions is being studied in detail using the PHOJET model by Engel [10,11]. We present here only a few comparisons of PHOJET results with hadron-hadron and photon-hadron data in order to illustrate, that the model as formulated in PHOJET is very well able to describe these channels. This is certainly required if we want to apply the model to photon-photon reactions, where nearly no experimental data are available. For photon-photon collisions we have to rely on the predictive power of the model.

A. Hadron-hadron collisions

In Figs. 5 and 6 we compare the transverse momentum distributions and pseudorapidity distributions with the results from collider experiments [44,45]. The rise of the plateau with the collision energy is understood within the model by one of its most important ingredients: The production of multiple soft interactions and multiple hard interactions (minijets) rises with energy. The transverse momentum distributions as measured at collider energies show in addition to the soft, exponentially damped, low-$p_\perp$ component of hadron production the rise of the perturbative hard component with increasing energy. This becomes more and more important with rising energy for minimum-bias hadron production.

Discussing the changes in hadron production with rising energy, we should indicate that PHOJET in its present version should not be applied for hadron-hadron, photon-hadron, or photon-photon collisions at collision energies beyond $\sqrt{s}=1$ to 2 TeV. PHOJET uses so far an energy-independent $p_\perp$ cutoff for the minijets. It was demonstrated in [8] that for parton structure functions with a $1/x^{1.5}$ or similar singularity of the sea-quark and gluon distributions, this might lead to unphysical effects above $\sqrt{s} = 2$ TeV. One possible way of how to apply a model with minijets in the TeV energy region of future proton-proton supercolliders (introducing an energy-dependent minijet $p_\perp$ cutoff) has been implemented in DTUJET-93 [8]. This could also be done in PHOJET, but is not necessary presently; photon-hadron or photon-photon collisions in the multi-TeV energy range seem not to be foreseen for the near future.

In Figs. 7 and 8 we compare PHOJET calculations to data on longitudinal distributions in the fragmentation region using the Feynman scaling variable x_F. Feynman x_F distributions have so far only been measured at fixed target energies, at laboratory energies well below 1 TeV. It has been shown

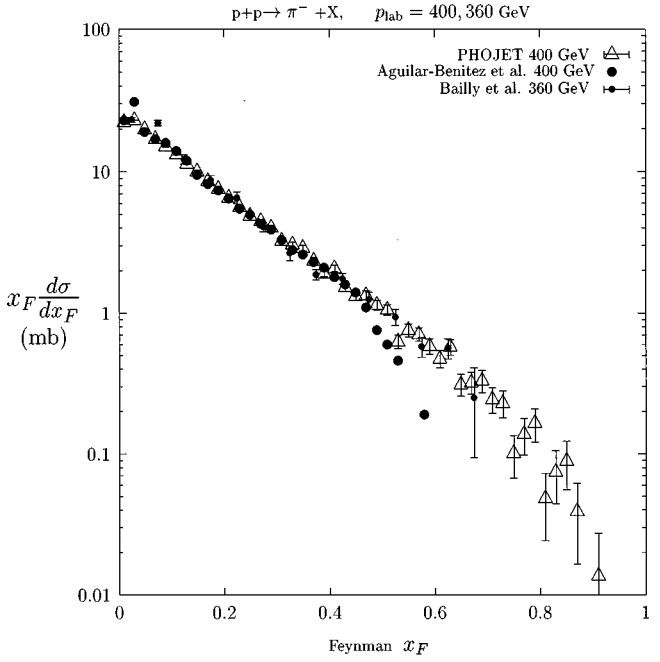

FIG. 8. Comparison of Feynman x_F distributions of π^- mesons produced in proton-proton collisions at 400 and 360 GeV. The experimental data are from the Aguilar-Benitez *et al.* [76] and from the EHS-RCBC Collaboration [77]. The data from both experiments agree rather well with each other; in fact, most of the data points of [77] are below the [76] data. The calculation uses the dual parton model PHOJET.

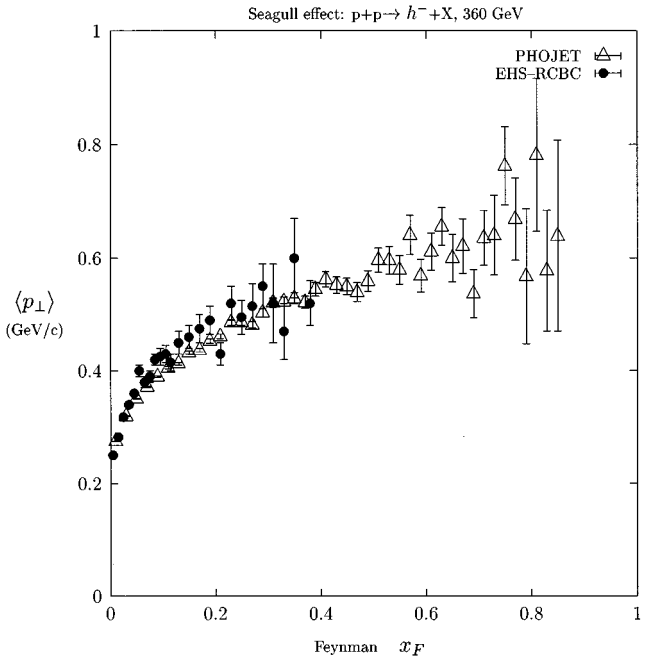

FIG. 9. Comparison of the seagull effect in the reaction $p+p \rightarrow h^- + \mathrm{X}$ at 360 GeV. The data are from the EHS-RCBC Collaboration [46]. The calculation uses the dual parton model PHOJET.

elsewhere [43] that the dual parton model shows outside the central region (rise of plateau) and the very forward fragmentation region (where the diffractive component is dominating) a very good Feynman scaling behavior.

The seagull effect, where one plots the average transverse momentum $\langle p_\perp \rangle$ as a function of Feynman x_F, demonstrates clearly that the distributions in transverse momentum and longitudinal momentum are correlated in a nontrivial way. There is no factorization between the transverse momentum and longitudinal momentum distributions, as is often assumed in oversimplified models of hadron production. In Fig. 9 we compare the seagull effect calculated with PHOJET to data measured in p_{lab}=360 GeV/c proton-proton collisions [46].

B. Photon-hadron collisions

The model for photon-hadron collisions is studied in full detail by Engel [11]. Here we present only some of this material in order to make the present paper self-contained.

In Fig. 10 we compare the transverse momentum distribution of charged hadrons calculated with PHOJET for photon-proton collisions with the photon laboratory energy E_γ=140 GeV with data from the OMEGA Collaboration [47]. The data were obtained with a tagged photon beam in the energy band 110–170 GeV. The agreement of both distributions is excellent; at the largest $p_\perp$ we see already the influence of direct and resolved hard collisions.

In Figs. 11 and 12 we compare PHOJET results with data from the HERA electron-proton collider [48]. In Fig. 11 we find a very good agreement with the transverse momentum

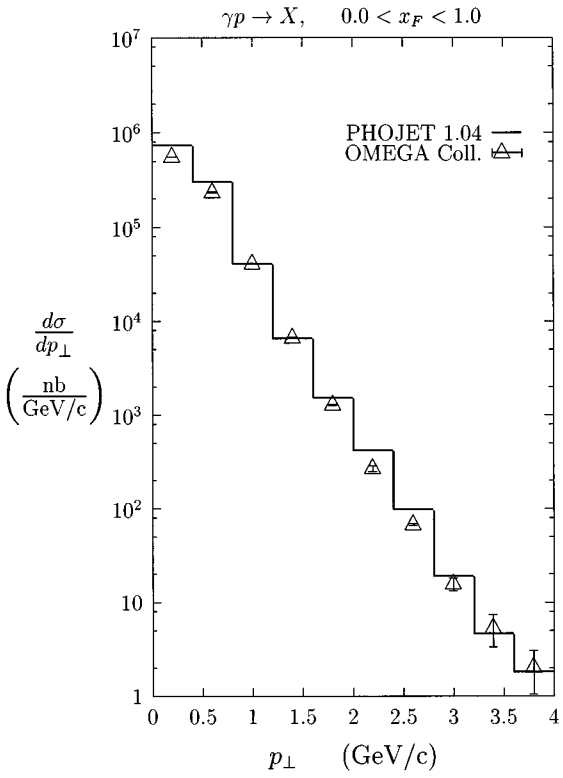

FIG. 10. Comparison of the transverse momentum distribution of charged hadrons with $0 \leqslant x_F \leqslant 1$ as calculated with PHOJET at the average photon energy of 140 GeV with data. The data are from the OMEGA Collaboration [47] measured with a tagged photon beam in the energy band 110–170 GeV.

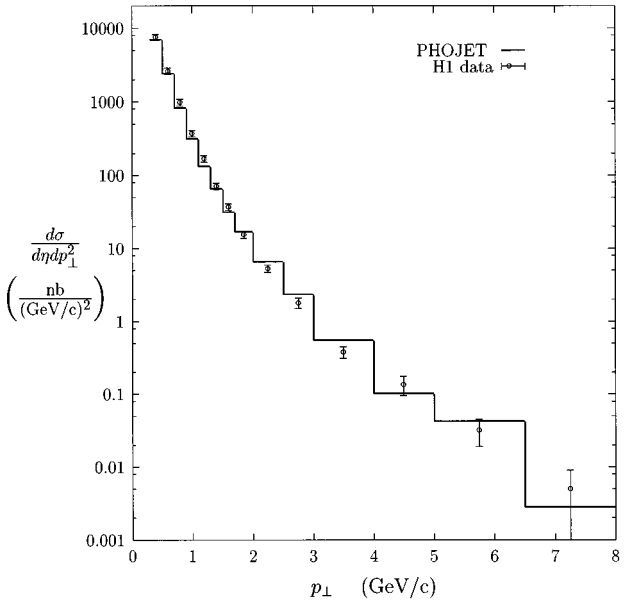

FIG. 11. Comparison of the transverse momentum distribution of charged hadrons produced by quasireal photons in electron-proton collisions at HERA [48] with the PHOJET calculation [10]. The data and the calculation are in the pseudorapidity region $-1.5 \leqslant \eta_{\text{lab}} \leqslant 1.5$.

distribution of charged hadrons. If we compare to proton-proton collisions (Fig. 5) we observe that the influence of hard collisions in photon-proton collisions is more prominent than in proton-proton collisions. In Fig. 12 we find a good agreement of the inclusive charged hadron production cross section as function of the pseudorapidity. We stress that the data as well as the model show a flat pseudorapidity distribution.

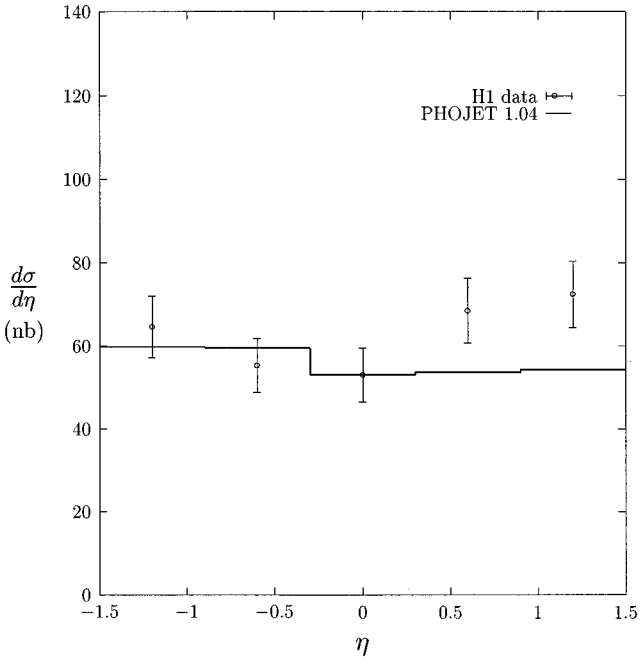

FIG. 12. Comparison of the inclusive pseudorapidity cross section of charged hadrons produced by quasireal photons in electron-proton collisions at HERA [48] with the PHOJET calculation [10].

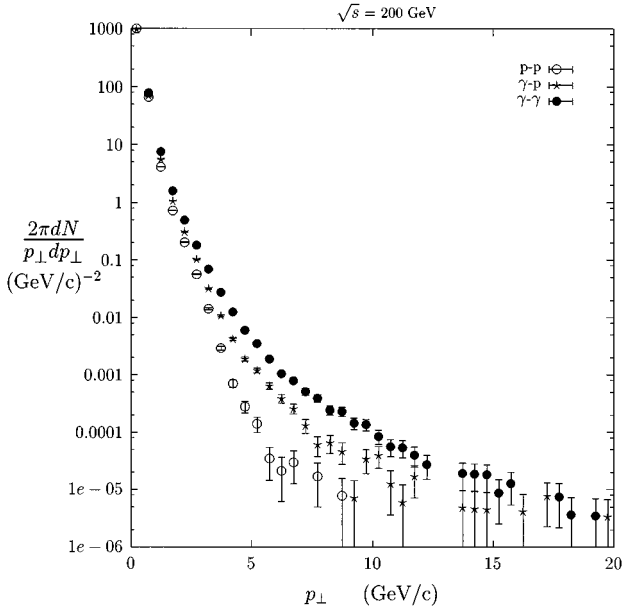

FIG. 13. We compare at the collision energy $\sqrt{s}=200$ GeV the transverse momentum distribution in invariant form for all charged hadrons produced in proton-proton, photon-proton, and photon-photon collisions. The calculation was done with PHOJET for inelastic collisions, excluding in photon-proton collisions the V-p and in photon-photon collisions the V-V diffractive production of vector mesons $V=\rho$, ω, and ϕ.

IV. COMPARISON OF MINIMUM-BIAS HADRON PRODUCTION IN HADRON-HADRON, PHOTON-HADRON, AND PHOTON-PHOTON COLLISIONS

In this section we compare the model predictions for inelastic hadron production in proton-proton, photon-proton, and photon-photon collisions at fixed c.m.s. energies $\sqrt{s}$. This is the usual way to present data on hadron-hadron collisions at colliders or in fixed target experiments. Collisions of quasireal photons with protons at electron-proton colliders and photon-photon collisions at electron-positron colliders are not at fixed photon-proton or photon-photon energy. We will discuss photon-photon collisions at electron-positron colliders in the next section. If we consider the three reaction channels at fixed energy, we do so only in order to find the characteristic differences and similarities between the three types of collisions. Since elastic hadron-hadron collisions usually are excluded studying inclusive secondary distributions, again, in order to find the similarities, we also exclude in the reactions with photons the corresponding quasielastic diffractive channel, i.e., $\gamma+\gamma \rightarrow V+V$ $(V=\rho,\omega,\phi)$, but we include all the other diffractive processes.

We start with the distribution, where the three channels differ most strongly, the transverse momentum distribution $dN/p_\perp dp_\perp$; see Fig. 13. The difference is striking. As first discussed by Schuler and Sjöstrand [12,13], the fraction of hard interactions in minimum bias interactions rises from proton-proton collisions over photon-proton collisions to photon-photon collisions. The reason for this is the direct photon interaction and the fact that the photon structure function is considerably harder than the proton structure function. In photon-photon collisions it is easy to observe already with

TABLE I. Comparison of average quantities characterizing hadron production in nondiffractive p-p, γ-p, and γ-γ collisions at c.m.s. energies between 10 and 200 GeV. The energies are given in GeV and average transverse momenta are given in GeV/c.

$\sqrt{s}$	Quantity	p-p	γ-p	γ-γ
10	n_{tot}	11.2	11.1	11.7
10	n_{ch}	6.65	6.53	6.86
10	n_{π^-}	2.17	2.44	2.88
10	$n_{\bar{p}}$	0.027	0.063	0.11
10	$\langle p_{\perp \text{ch}} \rangle_{\text{centr } \eta}$	0.39	0.38	0.42
10	$\langle p_{\perp} \rangle_{\pi^-}$	0.32	0.33	0.36
10	$\langle p_{\perp} \rangle_{\bar{p}}$	0.41	0.43	0.47
10	$\langle n \rangle_{\text{soft ch}}$	1.16	1.19	1.22
10	$\langle n \rangle_{\text{minijets}}$	0	0.00004	0.0020
20	n_{tot}	16.4	16.6	17.1
20	n_{ch}	9.64	9.71	10.00
20	n_{π^-}	3.44	3.78	4.18
20	$n_{\bar{p}}$	0.086	0.14	0.20
20	$\langle p_{\perp \text{ch}} \rangle_{\text{centr } \eta}$	0.37	0.38	0.44
20	$\langle p_{\perp} \rangle_{\pi^-}$	0.32	0.34	0.38
20	$\langle p_{\perp} \rangle_{\bar{p}}$	0.42	0.45	0.52
20	$\langle n \rangle_{\text{soft ch}}$	1.26	1.33	1.31
20	$\langle n \rangle_{\text{minijets}}$	0.0003	0.0025	0.028
50	n_{tot}	24.8	26.5	26.9
50	n_{ch}	14.5	15.5	15.6
50	n_{π^-}	5.49	6.19	6.53
50	$n_{\bar{p}}$	0.21	0.27	0.34
50	$\langle p_{\perp \text{ch}} \rangle_{\text{centr } \eta}$	0.38	0.40	0.46
50	$\langle p_{\perp} \rangle_{\pi^-}$	0.33	0.35	0.40
50	$\langle p_{\perp} \rangle_{\bar{p}}$	0.44	0.47	0.57
50	$\langle n \rangle_{\text{soft ch}}$	1.50	1.68	1.44
50	$\langle n \rangle_{\text{minijets}}$	0.0096	0.035	0.17
200	n_{tot}	40.1	46.2	47.5
200	n_{ch}	23.3	26.9	27.6
200	n_{π^-}	9.16	10.94	11.46
200	$n_{\bar{p}}$	0.46	0.59	0.67
200	$\langle p_{\perp \text{ch}} \rangle_{\text{centr } \eta}$	0.40	0.42	0.48
200	$\langle p_{\perp} \rangle_{\pi^-}$	0.35	0.38	0.42
200	$\langle p_{\perp} \rangle_{\bar{p}}$	0.47	0.53	0.64
200	$\langle n \rangle_{\text{soft ch}}$	1.59	1.87	1.29
200	$\langle n \rangle_{\text{minijets}}$	0.17	0.36	1.01

moderate statistics hadrons with transverse momenta close to the kinematic limit.

However, these differences in the hard scattering do not strongly influence such average properties of the collision as average multiplicities or even average transverse momenta. This can be seen from Table I, where we collect some average quantities characterizing nondiffractive proton-proton, proton-photon, and photon-photon collisions at c.m.s. energies between 10 and 200 GeV. The total and charged multiplicities at all energies are rather near to each other in all channels. Probably the differences in the multiplicities of hadrons such as π^- and $\bar{p}$ are more significant; we find them at all energies rising from p-p over γ-p to γ-γ collisions. Also the average transverse momenta rise as expected from

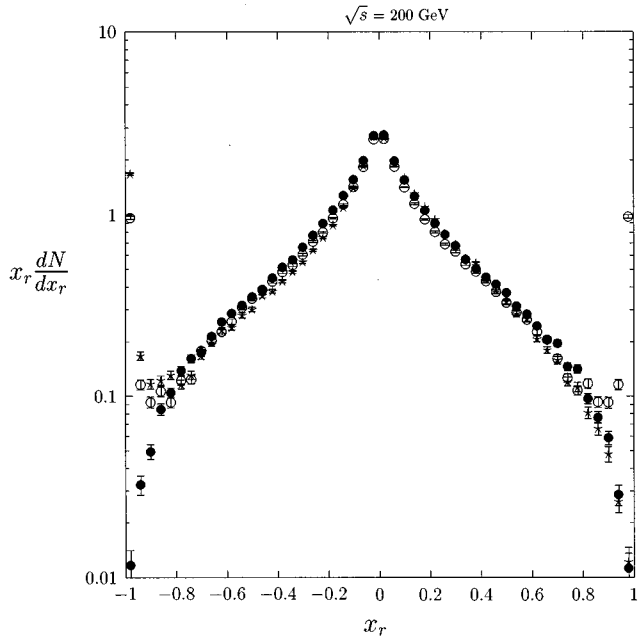

FIG. 14. We compare at the collision energy $\sqrt{s}=200$ GeV the x_r distribution in invariant form for all charged hadrons produced in proton-proton, photon-proton, and photon-photon collisions. The calculation was done with PHOJET for inelastic collisions, excluding in photon-proton collisions the V-p and in photon-photon collisions the V-V diffractive contributions.

p-p over γ-p to γ-γ. In Table I we give also the number of soft Pomerons, $\langle n \rangle_{\text{soft ch}}$, and the number of hard Pomerons, $\langle n \rangle_{\text{minijets}}$, contributing in average to the hadronic final state. The numbers given are obtained after kinematical corrections due to energy-momentum conservation, not the numbers obtained from the unitarization step (it turns out, especially at low energies, that for kinematical reasons not all sampled Pomeron cuts can be generated in the Monte Carlo simulation). At low energy, where the number of minijets is very small, we find the number of cut soft Pomerons to be the same in all three channels. The number of cut hard Pomerons rises at all energies from p-p over γ-p to γ-γ. We see also that the numbers of cut soft and cut hard Pomerons are correlated, and at high energies the number of cut soft Pomerons decreases from p-p over γ-p to γ-γ.

In Fig. 14 we compare the longitudinal momentum distributions in the form of $x_r dN/dx_r$ for the three channels. $x_r=(p_\parallel/|p_\parallel|)2E/\sqrt{s}$ is the so-called radial scaling variable, very similar to the Feynman variable $x_F=2p_\parallel/\sqrt{s}$. Significant differences between the three channels are only found in the region near $x_r = 1$ or -1. The reason is the single diffractive component, which in the p-p and γ-p case leads to the diffractive protons, which are obviously missing in γ-γ collisions.

In Fig. 15 we compare the seagull effect in the three channels. We find that as a result of the direct processes in photon-photon collisions, the rise of $\langle p_\perp \rangle$ with rising Feynman x_F is more prominent in photon-photon collisions than in proton-proton collisions. In photon-proton interactions we find in the proton fragmentation region agreement with the p-p collision, and in the photon fragmentation region, agreement with photon-photon collisions.

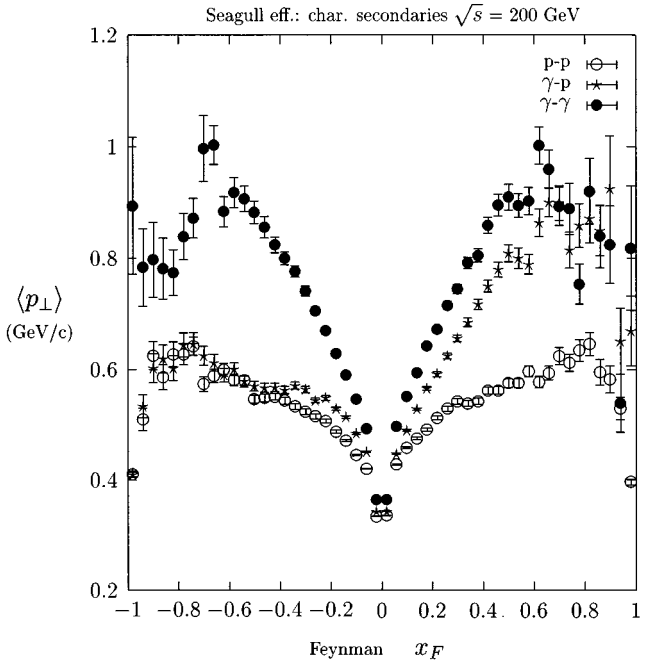

FIG. 15. We compare at the collision energy $\sqrt{s}=200$ GeV the average transverse momentum of charged hadrons produced in proton-proton, photon-proton, and photon-photon collisions as function of the Feynman x_F variable (seagull effect). The calculation was done with PHOJET for inelastic collisions, excluding in photon-proton collisions the V-p and in photon-photon collisions the V-V diffractive contributions.

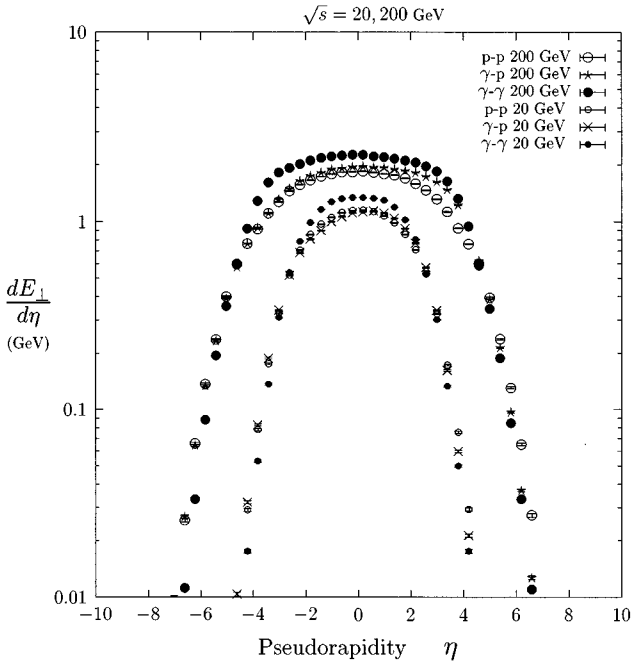

FIG. 16. We compare at the collision energies $\sqrt{s}=20$ GeV and 200 GeV the distribution of the transverse energy $E_\perp$ as function of the pseudorapidity η for proton-proton, photon-proton, and photon-photon collisions. The calculation was done with PHOJET for inelastic collisions, excluding in photon-proton collisions the V-p and in photon-photon collisions the V-V diffractive contributions.

In Fig. 16 we plot the transverse energy distribution $dE_\perp/d\eta$. Roughly, these distributions should be equivalent to the pseudorapidity distribution $dN/d\eta$ multiplied by the average transverse energy per particle. We observe characteristic differences, which can be understood from the features already discussed. At high energies we find the transverse energy distribution to be wider in photon-photon collisions than in proton-proton collisions. For instance, at 200 GeV we find the full width at half maximum (FWHM) of the curves rising from p-p over γp to γ-γ (7.60, 7.82, and 7.95 pseudorapidity units), similar at 1000 GeV (9.50, 10.10, and 10.6 pseudorapidity units). At low energies, the situation is less clear, at 20 GeV, the FWHM is smallest for γ-γ collisions. The transverse energy distribution rises at all η from p-p over γ-p to γ-γ. For γ-p the distribution agrees backwards with p-p and forwards with γ-γ.

For p-p or $\bar{p}$-p collisions the transverse energy distribution at $\eta=0$ is known from Intersecting Storage Rings (ISR) experiments and experiments at the CERN collider. The values calculated with PHOJET agree well with these measurements. At the DESY ep collider HERA it was found that practically the same transverse energy at $\eta = 0$ is found as in p-p interactions and in collisions of real or virtual photons with protons [49]. This observation agrees well with our results in Fig. 16.

Finally in Fig. 17 we plot the transverse energy distributions $dN_{\rm jet}/dE_{\perp\rm jet}$ of jets found in the Monte Carlo events from PHOJET. The jets are searched on the hadron level using a cone-jet-finding algorithm with the cone radius $R=\sqrt{(\Delta\eta)^2+(\Delta\varphi)^2}=1$. We find, again, that high $E_{\perp\rm jet}$ jets are more prominent in γ-γ collisions.

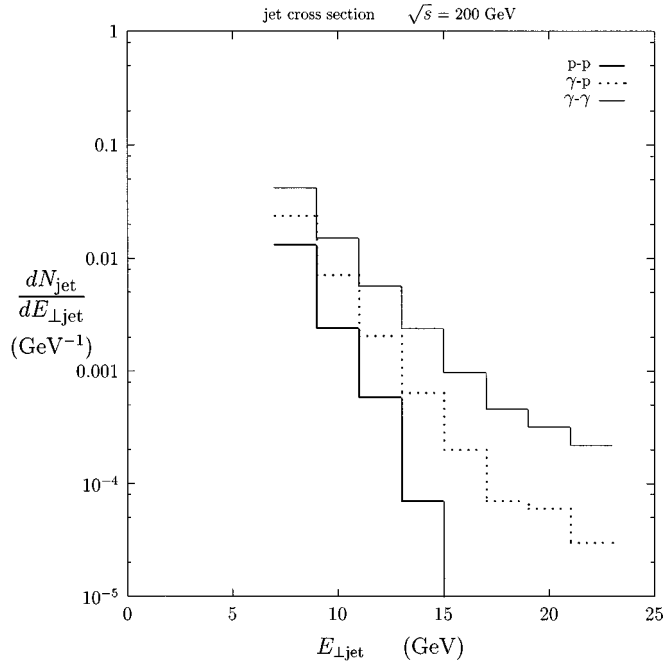

FIG. 17. We compare at the collision energy $\sqrt{s}=200$ GeV the transverse energy distribution for hadronic jets (identified using a jet-finding algorithm) produced in proton-proton, photon-proton, and photon-photon collisions. The calculation was done with PHOJET.

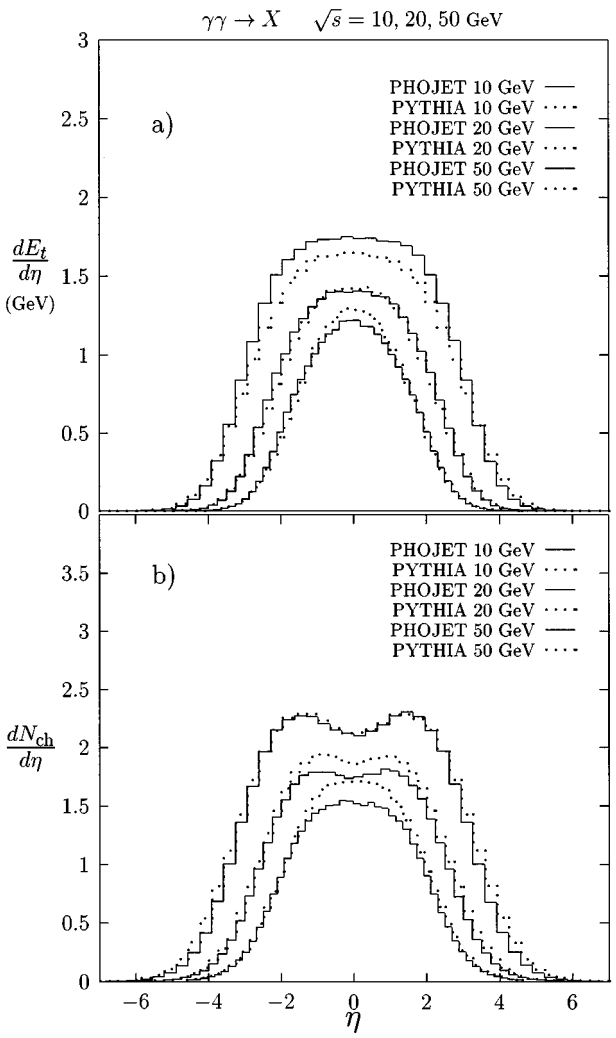

FIG. 18. Comparison of PYTHIA and PHOJET predictions on (a) the transverse energy flow vs pseudorapidity $dE_t/d\eta$ and (b) the pseudorapidity distribution $dN_{ch}/d\eta$ of charged particles in nonsingle diffractive events.

In the photon-photon reaction and at high enough energy, where such models work reliably in p-p collisions, there is not enough information from experiments on inclusive hadron distributions and jet production cross sections. Therefore, it might be interesting to compare the predictions from completely independent models with each other; this could be considered as a way to estimate the systematic uncertainties of the models. The PYTHIA model is a suitable model to compare our results with. Such comparisons were already presented for the energy region of the CERN e^+e^- collider LEP 2 in [50]. Here, we compare inclusive hadron production in nonsingle diffractive photon-photon collisions with $\sqrt{s}=10$, 20, and 50 GeV. A comparison of the predictions on jet distribution at LEP-II is given in the following section. The two models differ in the photon structure functions used [PHOJET uses the GRV leading order (LO) photon structure function [19]; PYTHIA uses the Schuler-Sjöstrand (SS) 1D photon structure function [51]]. Furthermore, the methods to construct the underlying soft hadronic event are completely different in both models. Therefore we might expect the largest differences in resolved events, which depend on the photon structure function and to which soft spectator jets contribute. In Figs. 18 and 19, the predictions on the transverse energy flow vs pseudorapidity, the transverse momentum distribution and the pseudorapidity distribution of charged particles are shown. The differences in the predictions of both models—and this is true for all three comparisons—are not negligible, but still reasonably small. These differences reflect certainly the differences in the methods to construct the soft part of the hadronic events.

V. HADRON AND JET PRODUCTION IN PHOTON-PHOTON COLLISIONS AT PRESENT AND FUTURE ELECTRON-POSITRON COLLIDERS

A. Photon flux calculation

1. Bremsstrahlung

The flux of weakly virtual photons is calculated taking into account only transversely polarized photons. Within this approximation the $ep \to eX$ photoproduction cross section is given by

$$\frac{d\sigma_{ep}}{dy\,dP^2} = f_{\gamma,e}(y,P^2)\,\sigma_{\gamma p}(s,P^2), \tag{23}$$

with

$$f_{\gamma,e}(y,P^2) = \frac{\alpha_{\rm em}}{2\pi P^2}\left[\frac{1+(1-y)^2}{y} - 2m_e^2 y\frac{1}{P^2}\right]. \tag{24}$$

Here, y and $P^2 = -p_\gamma^2$ denote the energy fraction taken by the photon from the electron and the photon virtuality. m_e is the electron mass. Neglecting the dependence of the γp cross section on P^2 in Eq. (23), the well-known equivalent photon approximation [26] is obtained:

$$f_{\gamma,e}(y,P^2) = \frac{\alpha_{\rm em}}{2\pi}\left[\frac{1+(1-y)^2}{y}\ln\frac{P^2_{\rm max}}{P^2_{\rm min}} - 2m_e^2 y\left(\frac{1}{P^2_{\rm min}} - \frac{1}{P^2_{\rm max}}\right)\right]. \tag{25}$$

For example, taking the kinematic limit $P^2_{\rm min,kin}$ as the lowest photon virtuality allowed,

$$P^2_{\rm min,kin} = \frac{m_e^2 y^2}{1-y}, \tag{26}$$

this simplifies to

$$f_{\gamma,e}(y) = \frac{\alpha_{\rm em}}{2\pi}\left(\frac{1+(1-y)^2}{y}\ln\frac{(1-y)}{m_e^2 y^2}P^2_{\rm max} - \frac{2(1-y)}{y}\right). \tag{27}$$

An expression similar to Eq. (23) is used for $ee \to ee + X$ scattering involving photons with small virtualities:

$$\frac{d^2\sigma_{ep}}{dy_1 dP_1^2 dy_2 dP_2^2} = f_{\gamma,e}(y_1,P_1^2)\,f_{\gamma,e}(y_2,P_2^2)\,\sigma_{\gamma\gamma}(s,P_1^2,P_2^2). \tag{28}$$

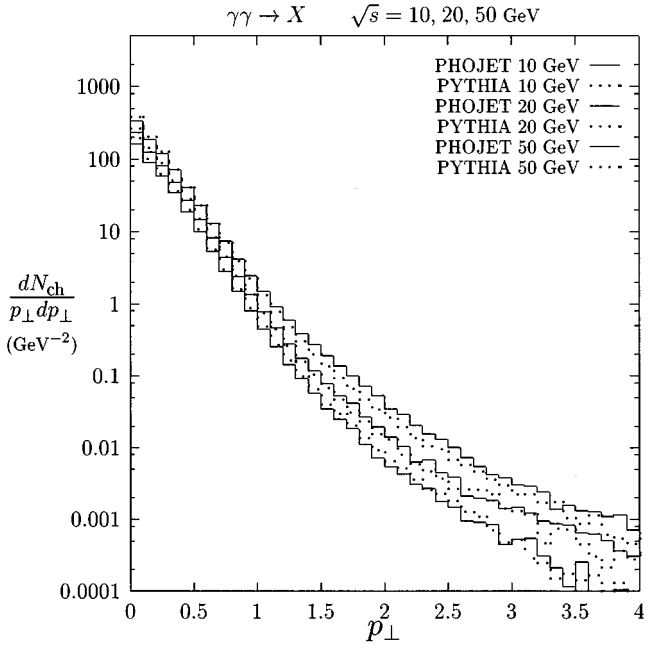

FIG. 19. Comparison of PYTHIA and PHOJET predictions on the transverse momentum distribution $dN_{ch}/dp_\perp$ of charged particles in nonsingle diffractive events.

2. Beamstrahlung

In the case of Gaussian beams, the effective beamstrahlung spectrum has been estimated by Chen *et al.* [52,53]. The dependence of this spectrum on the particle-bunch parameters can be expressed by the beamstrahlung parameter Υ:

$$\Upsilon = \frac{5 r_e^2 E N_e}{6 \alpha_{em} \sigma_z (\sigma_x + \sigma_y) m_e}. \tag{29}$$

Here, E denotes the beam energy, N_e is the number of electrons or positrons in a bunch, σ_x and σ_y are the transverse bunch dimensions, and $r_e = 2.818 \times 10^{-12}$ mm is the classical electron radius. The beamstrahlung spectrum is approximated by [53]

$$f_{\gamma,e}^{beam}(y) = \frac{\kappa^{1/3}}{\Gamma(1/3)} y^{-2/3} (1-y)^{-1/3} e^{-\kappa y/(1-y)} \times \left\{ \frac{1-w}{\tilde{g}(y)} \left[1 - \frac{1}{\tilde{g}(y) N_\gamma} (1 - e^{-N_\gamma \tilde{g}(y)}) \right] + w \left[1 - \frac{1}{N_\gamma} (1 - e^{-N_\gamma}) \right] \right\}, \tag{30}$$

with

$$\tilde{g}(y) = 1 - \tfrac{1}{2} (1-y)^{2/3} [1 - y + (1+y) \sqrt{1 + \Upsilon^{2/3}}], \tag{31}$$

$\kappa = 2/(3\Upsilon)$, and $w = 1/(6\sqrt{\kappa})$. The average number of photons, N_γ, emitted per electron is given by

$$N_\gamma = \frac{5 \alpha_{em}^2 \sigma_z m_e}{2 r_e E} \frac{\Upsilon}{\sqrt{1 + \Upsilon^{2/3}}}. \tag{32}$$

3. Photon emission by laser backscattering

Depending on the polarization of the laser light, various photon spectra can be produced [54–56]. Here we consider only the case of unpolarized laser radiation. Furthermore, we assume that the laser frequency is chosen to be below the pair-creation threshold at the optimal value given in [56]. Then, the spectrum of backscattered photons can be written as

$$f_{\gamma,e}^{laser}(y) = \frac{-0.544 y^3 + 2.17 y^2 - 2.63 y + 1.09}{(1-y)^2} \Theta(0.828 - y). \tag{33}$$

B. Comparison with data on jet production in photon-photon collisions at e^+e^- colliders

Data on hadron and jet production in collisions of quasireal photons have been reported by several experiments; see, for instance, [57–63]. A compilation of available data is given in [64]. Not all of these data are suitable to be compared with theoretical models without first performing a full detector simulation; for example, this is certainly the case for the data from [57–59], which are not acceptance corrected.

In this respect the cleanest, full acceptance-corrected data seem to be the jet transverse momentum distributions published by the TOPAZ and AMY Collaborations [62,63]. These data were already compared to next-to-leading-order QCD calculations by Aurenche *et al.* [30] and by Kleinwort and Kramer [65].

In Fig. 20 and we compare PHOJET results calculated using the GRV LO photon structure function [19] with the TOPAZ single-jet and two-jet transverse momentum distributions [62]. The TOPAZ antitag conditions and kinematical cuts were applied to the PHOJET events. The jets are searched from the Monte Carlo events on the hadron level using a cone-jet-finding algorithm with cone radius $R = 1$. The cross sections for these jets, which should approximately correspond to the jets identified in the experiment, are compared to the data. To illustrate the difference of these jet cross sections to the cross sections treating each hard parton ($p_\perp > 3$ GeV/c) as a single jet, we include in the figures also the nonfragmented parton cross sections. Both curves from the model differ considerably. The reason is the contribution of the underlying event to the $p_{\perp,jet}$ of the analyzed jets and the finite width of the hadonic jets. In some cases, the underlying event shifts the jet to larger pseudorapidities and therefore often out of the rapidity range of the data. Clearly, we should discuss the comparison of the data with the jet cross section found for the searched jets. The agreement is, however, not perfect; the model is below the data for the calculation using the GRV LO photon structure function [19]. It is interesting that the calculation of Kleinwort and Kramer [65], which uses the same GRV photon structure functions, shows the same disagreement to the single-jet data as found using PHOJET in Fig. 20.

The antitag condition of the AMY Collaboration [63] allows photons with rather large virtualities P^2; therefore, not only quasireal photons contribute to this data. We have to expect a less perfect agreement with a model for quasireal photon-photon collisions. This antitag condition also makes the data from the two experiments nonequivalent. In Fig. 21

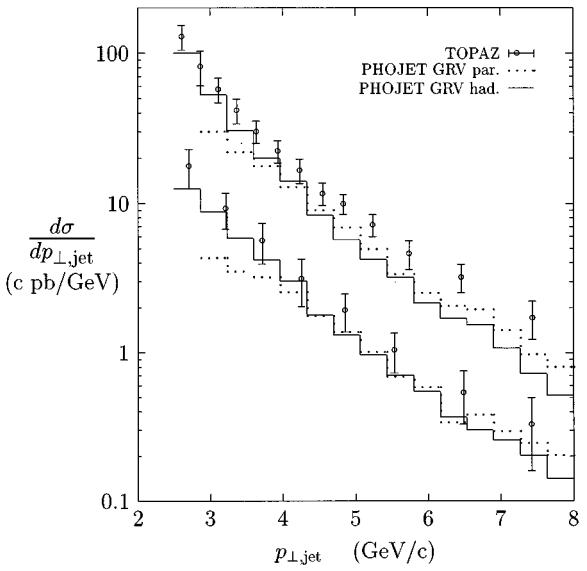

FIG. 20. Comparison of single-jet (upper curves) and two-jet (lower curves) cross sections from the TOPAZ Collaboration [62] with PHOJET results. PHOJET uses the GRV LO photon structure function [19]. We give from PHOJET the cross section corresponding to jets found using a jet-finding algorithm (these are the ones to be compared to the data) and in addition the cross sections on the parton level, without hadronization of the jets.

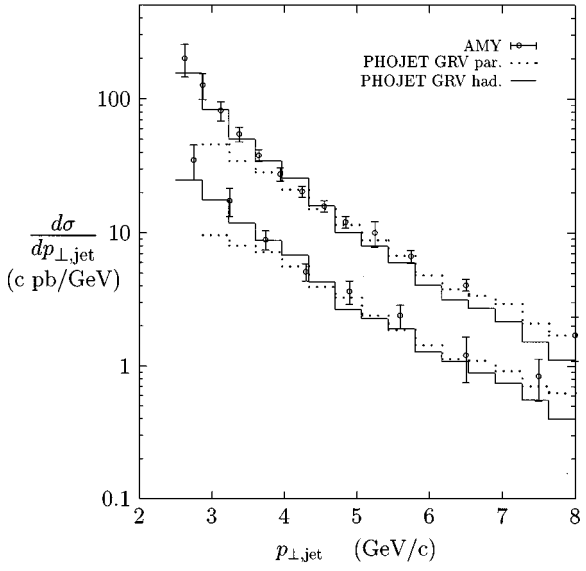

FIG. 21. Comparison of single-jet (upper curves) and two-jet (lower curves) cross sections from the AMY Collaboration [63] with PHOJET results. PHOJET uses the GRV LO photon structure function [19]. We give from PHOJET the cross section corresponding to jets found using a jet-finding algorithm (these are the ones to be compared to the data) and in addition the cross sections on the parton level, without hadronization of the jets.

we compare the PHOJET results, again treated with the antitag condition and kinematical cuts of the experiment, with the single- and two-jet data of the AMY Collaboration [63]. In fact, we find like Kleinwort and Kramer [65] a reasonable agreement (at least not worse than that to the TOPAZ data) to the AMY data. Similar results have been reported by Drees and Godbole [66] using a leading-order QCD calculation with several photon PDF's.

C. Hadron production in photon-photon collisions at future electron-positron linear colliders

Two-photon physics at future e^+e^- colliders has been discussed by several authors; for example, see [67,53]. These studies are mainly restricted to processes involving large momentum transfers. Here, we consider minimum-bias distributions which may be important for background estimations and detector design.

There are at present several projects for electron-positron linear colliders under active study. Here we pick out for our calculations only one of these projects, the TeV Energy Superconducting Linear Collider (TESLA). Details about the most recent TESLA project were given by Brinkmann [68].

Using the formulas discussed in the last subsection we plot in Fig. 22 the photon spectra according to the equivalent photon approximation, the beamstrahlung spectrum using the bunch parameters [68] as given in the caption of Fig. 22, and a backscattered laser spectrum. The photon virtuality was restricted to $P^2 \leqslant 0.01\ \mathrm{GeV}^2/c^2$. In Table II we give the average photon-photon energies and the cross sections in μb for the three photon spectra and two energies. From Fig. 22 and Table II we see that the beamstrahlung spectrum of the TESLA project is the softest of the three photon spectra and the backscattered laser spectrum is the hardest.

Of course, in the case of a linear collider we will always have to consider for background problems the superposition of the beamstrahlung spectrum and the bremsstrahlung spectrum.

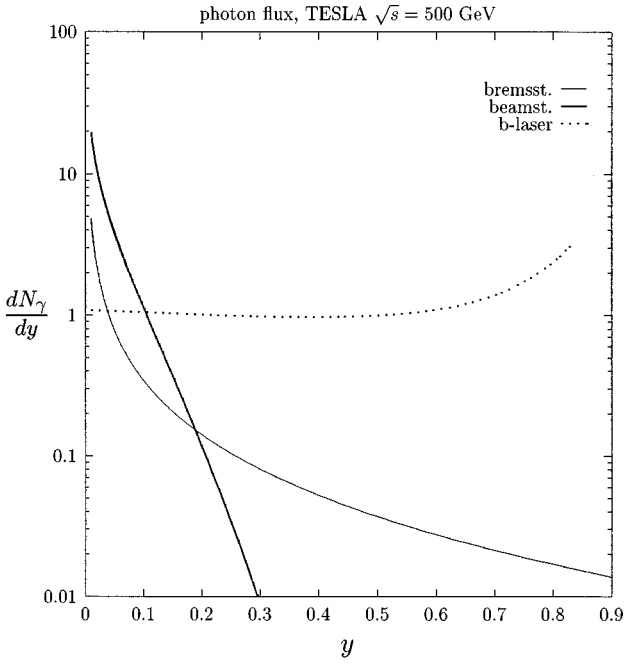

FIG. 22. Photon fluxes at a $\sqrt{s}$=500 GeV linear collider TESLA [68]. Given are the bremsstrahlung spectrum, the beamstrahlung spectrum using the bunch parameters $N_e = 1.8 \times 10^{10}$, σ_x=598 nm, σ_y=6.5 nm, and σ_z=0.5 mm [68], and a backscattered laser spectrum.

TABLE II. Average photon-photon energies and e^+e^- cross section in μb for the three photon spectra and two linear collider energies. The energies are given in GeV.

$\sqrt{s}_{e^+e^-}$	Photon spectrum	$\sqrt{s}_{\gamma\gamma}$	Weight (μb)
500	Bremsst.	50	0.0067
500	Beamst.	16.7	0.038
500	B.Laser	252	0.47
1000	Bremsst.	105	0.0075
1000	Beamst.	41	0.026
1000	B.Laser	509	0.59

A reasonable lowest energy for collisions to be sampled using PHOJET is $\sqrt{s}_{\gamma\gamma}=5$ GeV (PHOJET would, however, run without problems even down to $\sqrt{s}_{\gamma\gamma}=2$ GeV). For all applications in this and the following subsection we always cut the photon spectra at small y in such a way that this lower-energy cutoff is respected.

In Figs. 23 and 24 we plot the cross sections $\sigma dE_\perp/d\eta$ for the transverse energy as function of pseudorapidity and $d\sigma/d\eta$ for the charged hadron production as function of pseudorapidity. It is clearly visible that the backscattered laser spectrum is rather hard and has the highest weight. The beamstrahlung spectrum and the bremsstrahlung spectrum are rather comparable; the former has the higher weight, and the latter is the harder of these two.

The same differences between the three photon spectra are visible in the cross sections $d\sigma/dp_\perp$ for charged hadron production as function of the transverse momentum in Fig. 25 for the 500 GeV TESLA collider.

D. Hadron and jet production in photon-photon collisions at the LEP-II electron-positron collider

We use throughout this section an electron-positron energy of $\sqrt{s}=175$ GeV for phase II of the LEP collider. Of course, here we have only to consider the bremsstrahlung spectrum. Assuming antitagging of the scattered electrons and positrons we restrict the scattering angle of the outgoing electron and positron to $\theta_{\max}<40$ mrad. This is a realistic antitagging condition which can be achieved with the luminosity detectors at LEP. Since we are interested in jets, only events with $\sqrt{s}_{\gamma\gamma}>10$ GeV are considered. The average photon-photon energy at LEP-II with the given electron-positron energy will be $\sqrt{s}_{\gamma\gamma}\approx 27$ GeV. The virtuality P^2 of the photons will be about $\langle P^2\rangle\approx 0.1$ GeV^2. In Table III we compare some average properties of the LEP-II photon-photon collisions with photon-photon collisions at $\sqrt{s}_{\gamma\gamma}=25$ GeV. We find that the average properties are rather well represented by photon-photon collisions at $\sqrt{s}_{\gamma\gamma}=25$ GeV.

In the following we consider a calorimeter detector with the pseudorapidity coverage $|\eta|\leqslant 2.1$. Applying a jet finding algorithm to this detector we can identify jets in the pseudorapidity range $|\eta_{\rm jet}|\leqslant 1.1$. For the jets we use generally a lower jet transverse energy cutoff $E_{\perp\rm jet}\geqslant 5$ GeV.

In Fig. 26 we show the jet transverse energy distribution in the acceptance region given above together with its decomposition into the different hard interaction mechanisms.

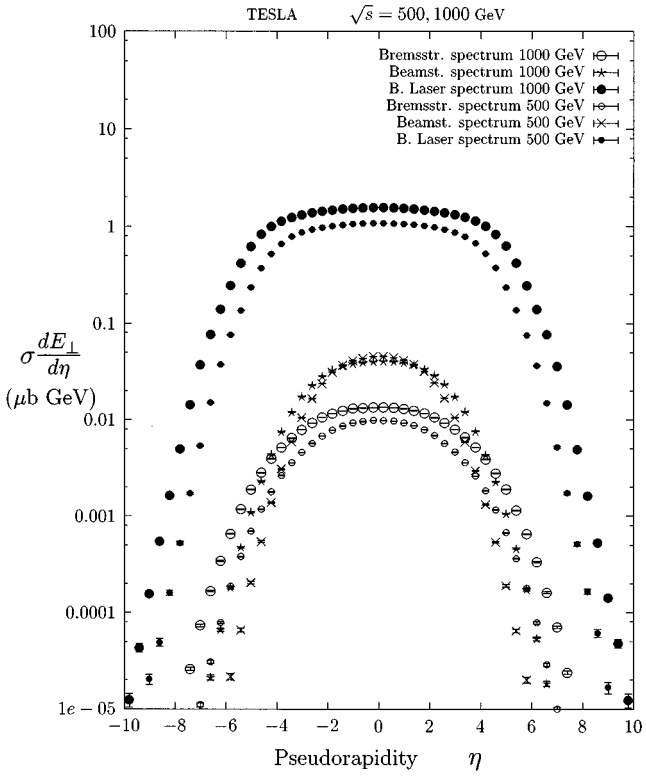

FIG. 23. Cross section weighted transverse energy distributions $\sigma dE_\perp/d\eta$ measured in μb GeV at the $\sqrt{s}=500$ and 1000 GeV TESLA linear colliders [68]. Given are the distributions for the bremsstrahlung photon spectrum, the beamstrahlung spectrum, and a backscattered laser spectrum.

The single-resolved contribution within the acceptance region is surprisingly small. At small $E_{\perp\rm jet}$, the double-resolved contribution dominates; at large $E_{\perp\rm jet}$, the direct contribution dominates.

One problem, which can only be studied with a model formulated as an event generator, is the difference between jets as calculated from the theory on the parton level and the jets obtained from a jet-finding algorithm from the hadronic events. There are essentially two effects: (i) In a detector with a limited acceptance region one gets a difference due to the finite width of the hadronized jets. (ii) If the jets are produced above a soft hadronic background, then this background will contribute randomly to the jets, increasing their transverse energy or increasing even the number of jets.

In Fig. 27 we study this problem separately for direct, single-resolved, and double-resolved jet events. The leading-order parton model cross section, taking each parton as a jet, is compared with the predictions of the full model, including initial and final state radiation and hadronization. The jet cross section of direct jets on hadron level is decreased against the ones on parton level. There is no underlying soft hadronic background in these events; the reduction is due to the width of the jets together with the limited jet cone used for the jet search and the limited detector acceptance. In the model, the jet width is determined by final state radiation and hadronization. In the case of double-resolved jet events, the opposite behavior is found. Double-resolved events are characterized by the largest soft hadronic background of the three interaction types considered here. This background together

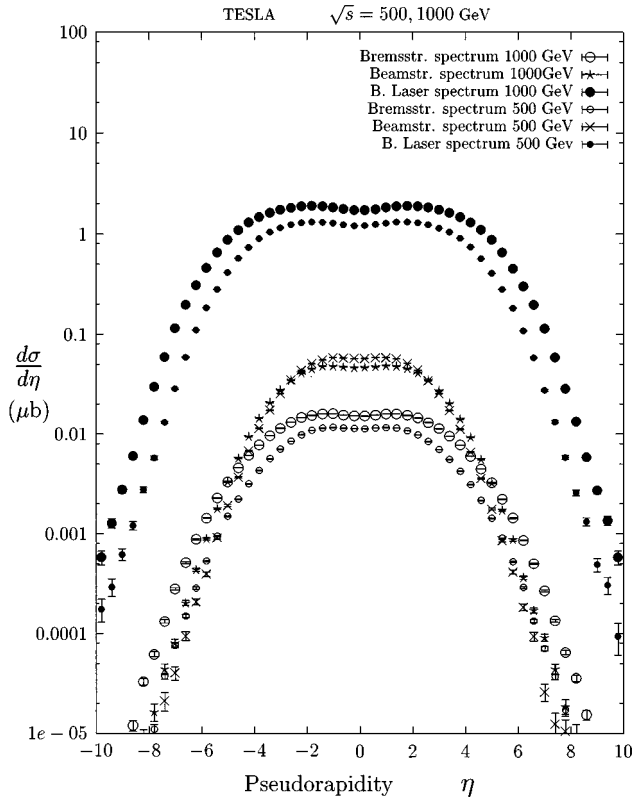

FIG. 24. Pseudorapidity cross sections $d\sigma/d\eta$, measured in μb per pseudorapidity unit, at the $\sqrt{s}$=500 and 1000 GeV TESLA linear colliders [68]. Given are the distributions for the bremsstrahlung spectrum, the beamstrahlung spectrum, and a backscattered laser spectrum.

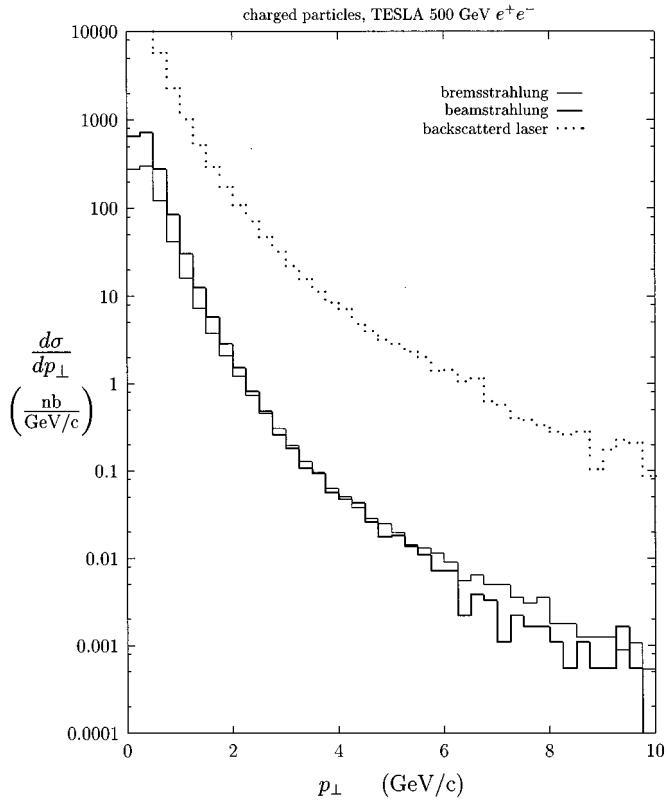

FIG. 25. Transverse momentum cross sections $d\sigma/dp_\perp$ at the $\sqrt{s}$=500 GeV TESLA linear collider [68]. Given are the distributions for the bremsstrahlung photon spectrum, the beamstrahlung spectrum, and a backscattered laser spectrum. Please note that the $p_\perp$ distributions for the bremsstrahlung spectrum and the beamstrahlung spectrum cross. At low $p_\perp$ the beamstrahlung dominates, at high $p_\perp$ the bremsstrahlung spectrum dominates.

with effects of initial state radiation and multiple interactions leads to a significant increase of the hadronic jet cross section against the partonic one. For single-resolved jets the soft background is less than for the double-resolved ones; also the contribution due to initial state radiation is smaller. We find that in this case the effects compensate approximately and the jet cross sections on hadron and parton levels are very near to each other.

To study the influence of multiple soft and multiple hard interactions in the model we plot in Fig. 28 the jet $E_\perp$ cross section for double-resolved events using the following model versions: (i) a model with single soft or hard interactions, (ii) a model with up to one soft and multiple hard interactions, and (iii) a full model with multiple soft and hard interactions. To realize model versions (i) and (ii), the number of soft and hard interactions is sampled according to Eq. (10); however, in events with more than one soft or hard interaction, the number of interactions is cut down to the limits given for (i) and (ii). The arbitrary threshold between soft and hard partons in the model is $p_\perp^{\text{cutoff}}=3$ GeV/c. The curve for (ii) is rather close to the $E_{\perp\text{jet}}$ distribution of the full model. With the average numbers of minijets given in Table III the chance to have more than one minijet in one event is small. This is different for the soft interactions; the chance to have in addition to the hard scattering at least one soft interaction is rather high.

An estimate of the model dependence of these predictions is obtained by comparing the results obtained with PHOJET and PYTHIA. To avoid any bias due to different photon flux approximations, the events have been generated with the photon flux function (24) as implemented in PHOJET, however using PYTHIA (with default parameter settings) for the simulation of the γ-γ scattering process. In Fig. 29 we present jet cross sections from both models in $\sqrt{s}_{e^+e^-}=175$ GeV photon-photon collisions separately for direct, single-

TABLE III. Comparison of average quantities for LEP-II photon-photon collisions with photon-photon collisions at $\sqrt{s}_{\gamma\gamma}=25$ GeV. The average transverse momenta are given in GeV/c.

Quantity	LEP-II $\gamma\gamma$	$\gamma\gamma$ at 25 GeV
n_{tot}	15.9	17.2
n_{ch}	9.58	10.1
n_{π^+}	3.98	4.12
n_{π^-}	3.98	4.12
$n_{\bar{p}}$	0.20	0.19
$\langle p_\perp \rangle_{\pi^-}$	0.37	0.37
$\langle p_\perp \rangle_{\bar{p}}$	0.48	0.50
$\langle n \rangle_{\text{soft ch}}$	1.21	1.44
$\langle n \rangle_{\text{minijets}}$	0.030	0.028
Weight (μb)	0.0032	

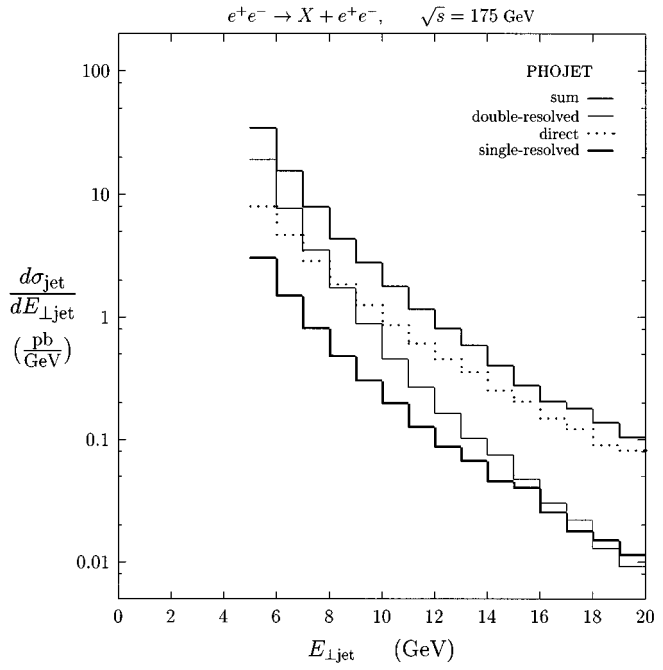

FIG. 26. Decomposition of the jet cross section $d\sigma_{\rm jet}/dE_{\perp\rm jet}$ as a function of the jet transverse energy. The jets with $E_{\perp\rm jet} \geqslant 5$ GeV were found from the PHOJET events using a cone algorithm. The jet acceptance region was restricted to $|\eta_{\rm jet}| \leqslant 1.1$. Note that the single-resolved contribution as shown enters the total jet cross section twice.

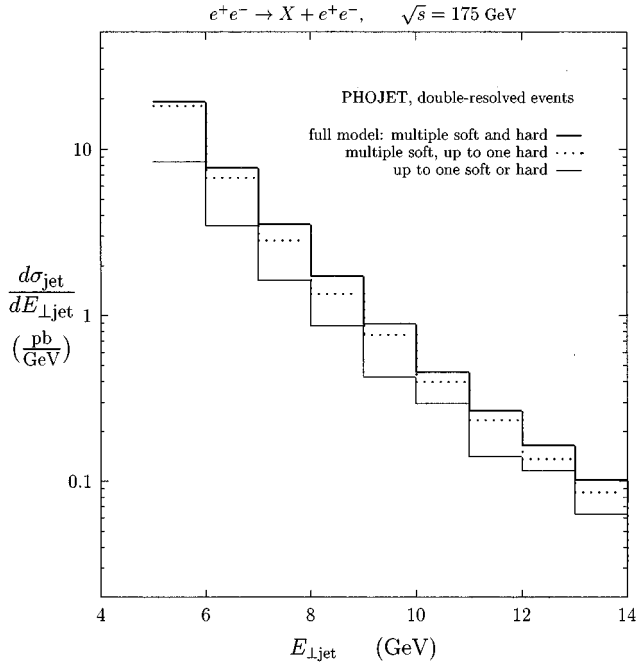

FIG. 28. Jet cross section $d\sigma_{\rm jet}/dE_{\perp\rm jet}$ as a function of the jet transverse energy. In order to study the influence of multiple soft and hard interactions in the model, we consider restricted cases with only single soft or single hard collisions. The curve with multiple soft, single hard collisions coincides nearly with the solid curve. The jets with $E_{\perp\rm jet} \geqslant 5$ GeV were found from the PHOJET events using a cone algorithm. The jet acceptance region was restricted to $|\eta_{\rm jet}| \leqslant 1.1$.

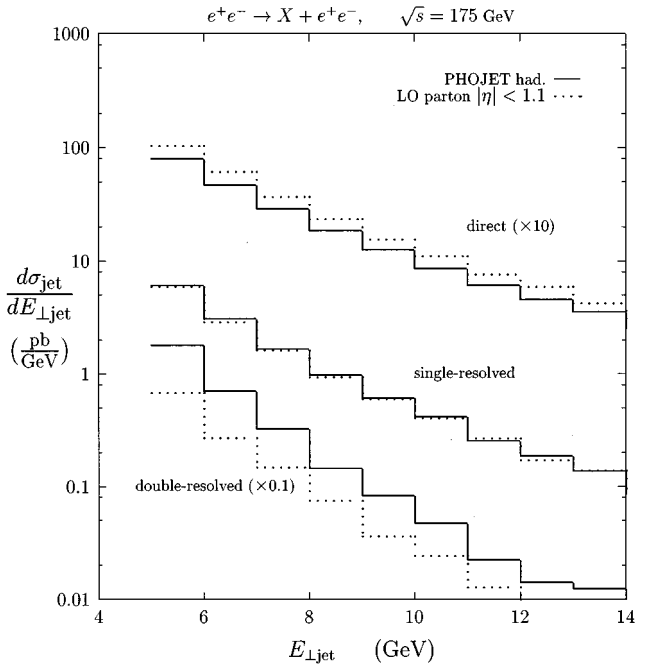

FIG. 27. Jet cross section $d\sigma_{\rm jet}/dE_{\perp\rm jet}$ of direct, single-resolved, and double-resolved interactions as a function of the jet transverse energy. For partonic as well as hadronic jets, the acceptance region was restricted to $|\eta_{\rm jet}| \leqslant 1.1$.

resolved, and double-resolved events. As expected, we find nearly no differences for direct events and the differences are largest in double-resolved events. However, for transverse jet energies above 8 GeV the differences between both models are rather small. Switching off multiple interactions in PHOJET, both models give similar predictions.

To study the influence of an upper visible energy cut we plot in Fig. 30 the jet transverse energy cross section together with the distribution obtained with the cut $E_{\rm visible} \leqslant 50$ GeV within the acceptance region $|\eta| \leqslant 2.1$. The 50 GeV cut serves to suppress jets coming from Z^0 decay. For jets with transverse energies below 10 GeV this cut does not change the $E_{\perp\rm jet}$ distribution drastically. Finally, in Fig. 31 we plot the cross section as function of the visible energy within the acceptance region. Since we want to search jets with an $E_{\perp\rm jet} \geqslant 5$ GeV cutoff, we use a lower threshold for the photon-photon energy $\sqrt{s_{\gamma\gamma}} = 10$ GeV. The plot gives the visible energy distribution without restrictions and in a second curve the visible energy is obtained if we demand at least one jet with $E_{\perp\rm jet} \geqslant 5$ GeV and impose the visible energy cut $E_{\rm visible} \leqslant 50$ GeV within the acceptance region given above. We observe, that nearly each event with a visible energy above 30 GeV contains at least one jet with $E_{\perp\rm jet} \geqslant 5$ GeV.

VI. CONCLUSIONS AND SUMMARY

The PHOJET model can be used to calculate hadronic events in hadron-hadron, photon-hadron, and photon-photon collisions. The model is found to agree well with data in hadron-hadron and photon-hadron collisions; the predictions

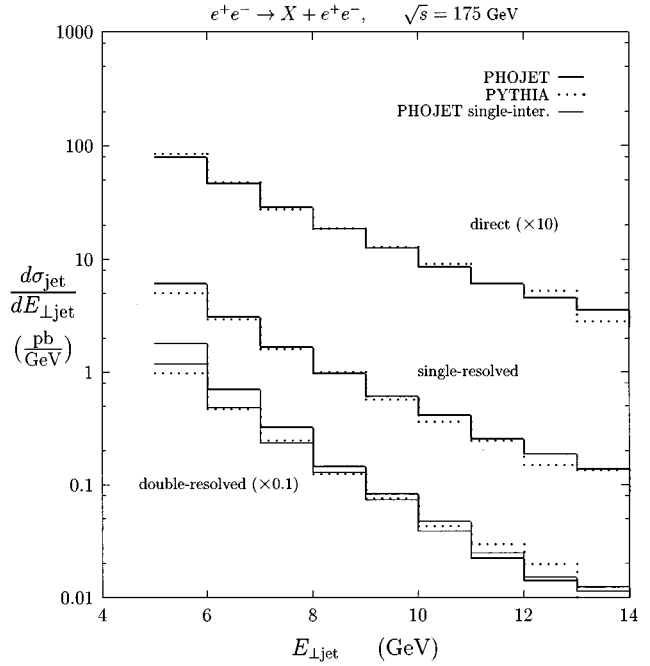

FIG. 29. Comparison of PYTHIA and PHOJET predictions on the jet cross sections $d\sigma_{\rm jet}/dE_{\perp\rm jet}$ as a function of the jet transverse energy. The contributions of the three basic interaction types, direct, single-resolved, and double-resolved, are shown separately. For the calculations, the photon PDF parametrizations GRV LO and SaS 1D have been used for PHOJET and PYTHIA, respectively.

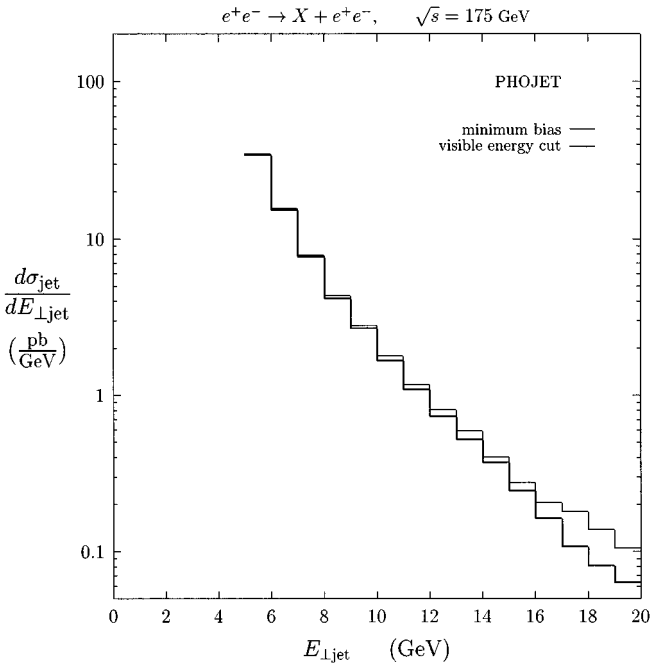

FIG. 30. Jet cross section $d\sigma_{\rm jet}/dE_{\perp\rm jet}$ as a function of the transverse energy. Here we give in addition the cross section with a visible energy cut (inside a calorimeter with $|\eta| \leqslant 2.1$ the cut is $E_{\rm vis} \leqslant 50$ GeV). The jets with $E_{\perp\rm jet} \geqslant 5$ GeV were found from the PHOJET events using a cone algorithm. The jet acceptance region was restricted to $|\eta_{\rm jet}| \leqslant 1.1$.

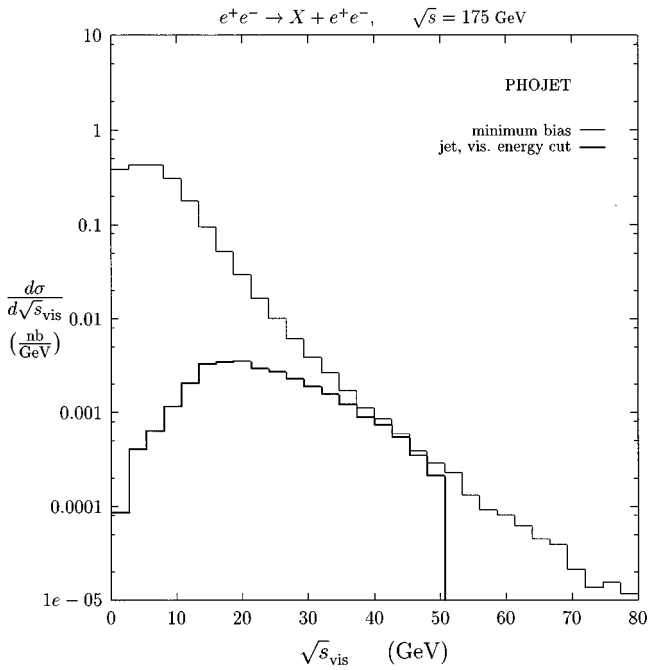

FIG. 31. Cross section as a function of the visible energy inside a calorimeter with $|\eta| \leqslant 2.1$. Only events with $\sqrt{s}_{\gamma\gamma} \geqslant 10$ GeV are sampled from the photon spectrum, Eq. (24). In a second curve we request jets with $E_{\perp\rm jet} \geqslant 5$ GeV and impose a visible energy cut of 50 GeV.

for photon-photon collisions do not need any new parameters.

Multiple soft and multiple hard interactions (minijets) lead to a rise of the rapidity plateau, which agrees in hadron-hadron and photon-hadron collisions very well with the rise of the plateau observed experimentally.

Minimum-bias hadron production in hadron-hadron, photon-hadron, and photon-photon collisions of the same c.m.s. energy is remarkably similar. To see this, one has to restrict the comparison to inelastic events and to exclude also the diffractively produced vector mesons in reactions involving photons. The only striking differences appear in the transverse momentum distribution or distributions, where the transverse momentum behavior is essential. This difference can be understood to be due to the direct photon interaction contribution and due to the photon structure function being considerably harder than hadronic structure functions.

PHOJET can be applied also to photon-photon interactions at electron-hadron and electron-electron or electron-positron colliders. Photon spectra according to bremsstrahlung, beamstrahlung and backscattered laser radiation in linear electron-positron colliders are implemented at present. The model shows reasonable agreement with data on jet production in photon-photon collisions as obtained by the TOPAZ and AMY Collaborations [62,63]. It is easy to implement other similar photon spectra. With these possibilities PHOJET should be a tool suitable to study the photon-photon background to other interesting reactions at such colliders.

After finalizing this work, we learned that Schuler and Sjöstrand had just issued a report [69] where they study hadronic photon-photon interactions using an alternative model.

As shown in Figs. 18, 19, and 29, the predictions of both models agree reasonably well.

ACKNOWLEDGMENTS

The authors are grateful to P. Aurenche for many helpful discussions and suggestions, and T. Sjöstrand for running PYTHIA in minimum-bias mode for comparison, and they acknowledge the invitations to sessions of LEP-II and linear collider study groups by the conveners of these studies. One of the authors (R.E.) thanks V.G. Serbo for useful discussions, he acknowledges the hospitality and support by LAPP Annecy-le-Vieux, where a large part of the results presented were obtained, and the support by the Deutsche Forschungsgemeinschaft under Contract No. Schi 422/1-2.

[1] A. Capella, U. Sukhatme, C. I. Tan, and J. Tran Thanh Van, Phys. Rep. **236**, 227 (1994).
[2] P. Aurenche, F. W. Bopp, A. Capella, J. Kwiecinski, M. Maire, J. Ranft, and J. Tran Thanh Van, Phys. Rev. D **45**, 92 (1992).
[3] A. Capella, J. Tran Thanh Van, and J. Kwiecinski, Phys. Rev. Lett. **58**, 2015 (1987).
[4] F. W. Bopp, A. Capella, J. Ranft, and J. Tran Thanh Van, Z. Phys. C **51**, 99 (1991).
[5] F. W. Bopp, D. Pertermann, and J. Ranft, Z. Phys. C **54**, 683 (1992).
[6] R. Engel, F. W. Bopp, D. Pertermann, and J. Ranft, Phys. Rev. D **46**, 5192 (1992).
[7] S. Roesler, R. Engel, and J. Ranft, Z. Phys. C **59**, 481 (1993).
[8] F. W. Bopp, R. Engel, D. Pertermann, and J. Ranft, Phys. Rev. D **49**, 3236 (1994).
[9] R. Engel, Z. Phys. C **66**, 203 (1995).
[10] R. Engel, in *Proceedings of the XXIXth Rencontre de Moriond*, edited by J. Trân Thanh Vân (Edition Frontieres, Gif-sur-Yvette, 1994), p. 321.
[11] R. Engel (in preparation).
[12] G. A. Schuler and T. Sjöstrand, Nucl. Phys. **B407**, 539 (1993).
[13] G. A. Schuler and T. Sjöstrand, in Proceedings of the Workshop on Two-Photon Physics from DAΦNE to LEP200 and beyond, Paris, France, edited by F. Kapusta and J. Parisi, Report No. CERN-TH.7193/94 (unpublished).
[14] T. Sjöstrand, Comput. Phys. Commun. **82**, 74 (1994).
[15] M. Baker and K. A. Ter-Martirosyan, Phys. Rep. **28C**, 1 (1976).
[16] B. L. Combridge, J. Kripfganz, and J. Ranft, Phys. Lett. **70B**, 234 (1977).
[17] D. W. Duke and J. F. Owens, Phys. Rev. D **26**, 1600 (1982).
[18] M. Glück, E. Reya, and A. Vogt, Phys. Rev. D **45**, 3986 (1992).
[19] M. Glück, E. Reya, and A. Vogt, Phys. Rev. D **46**, 1973 (1992).
[20] A. Capella, J. Kaplan, and J. Tran Thanh Van, Nucl. Phys. **B105**, 333 (1976).
[21] J. C. Collins and G. A. Landinsky, Phys. Rev. D **43**, 2847 (1991).
[22] R. S. Fletcher, T. K. Gaisser, and F. Halzen, Phys. Rev. D **45**, 377 (1992).
[23] J. R. Forshaw and J. K. Storrow, Phys. Rev. D **46**, 4955 (1992).
[24] V. A. Abramovski, V. N. Gribov, and O. V. Kancheli, Yad. Fiz. **18**, 595 (1973) [Sov. J. Nucl. Phys. **18**, 308 (1973)].
[25] K. A. Ter-Martirosyan, Phys. Lett. **44B**, 377 (1973).
[26] V. M. Budnev, I. F. Ginzburg, G. V. Meledin, and V. G. Serbo, Phys. Rep. **15C**, 181 (1975).
[27] I. F. Ginzburg and V. G. Serbo, Phys. Lett. **109B**, 231 (1982).
[28] PLUTO Collaboration, C. Berger *et al.*, Phys. Lett. **89B**, 287 (1981).
[29] F. Borzumati and G. A. Schuler, Z. Phys. C **58**, 139 (1993).
[30] P. Aurenche, J. P. Guillet, M. Fontannaz, Y. Shimizu, and K. Kato, Prog. Theor. Phys. **92**, 175 (1994).
[31] M. Drees and R. M. Godbole, Phys. Rev. D **50**, 3124 (1994).
[32] K. Hahn and J. Ranft, Phys. Rev. D **41**, 1463 (1990).
[33] T. Sjöstrand, Phys. Lett. **157B**, 321 (1985).
[34] T. Gottschalk, Nucl. Phys. **B277**, 700 (1986).
[35] E. Witten, Nucl. Phys. **B120**, 189 (1977).
[36] A. Capella, U. Sukhatme, and J. Tran Thanh Van, Z. Phys. C **3**, 329 (1980).
[37] A. Capella, U. Sukhatme, C. I. Tan, and J. Tran Thanh Van, Z. Phys. C **10**, 249 (1980).
[38] A. B. Kaidalov, Phys. Lett. **116B**, 459 (1982).
[39] A. B. Kaidalov and K. A. Ter-Martirosyan, Phys. Lett. **117B**, 247 (1982).
[40] A. Capella, A. Kaidalov, C. Merino, and J. Tran Thanh Van, Phys. Lett. B **343**, 403 (1995).
[41] R. Engel, J. Ranft, and S. Roesler, Phys. Rev. D **52**, 1459 (1995).
[42] H. U. Bengtsson, Comput. Phys. Commun. **31**, 323 (1984).
[43] J. Ranft, Phys. Rev. D **51**, 64 (1995).
[44] UA1 Collaboration, C. Albajar *et al.*, Nucl. Phys. **B335**, 261 (1990).
[45] UA5 Collaboration, G. J. Alner *et al.*, Z. Phys. C **33**, 1 (1986).
[46] EHS-RCBC Collaboration, J. L. Bailly *et al.*, Z. Phys. C **35**, 295 (1987).
[47] OMEGA Photon Collaboration, R. J. Apsimon *et al.*, Z. Phys. C **43**, 63 (1989).
[48] H1 Collaboration, I. Abt *et al.*, Phys. Lett. B **328**, 177 (1994).
[49] H1 Collaboration, S. Aid *et al.*, Z. Phys. C **70**, 17 (1995).
[50] Report from the working group on $\gamma\gamma$ physics, in Proceedings of the LEP 2 workshop, edited by G. Altarelli and T. Sjöstrand, Report No. CERN 96-01 (unpublished).
[51] G. A. Schuler and T. Sjöstrand, Z. Phys. C **68**, 607 (1995).
[52] P. Chen, Phys. Rev. D **46**, 1186 (1992).
[53] P. Chen, T. L. Barklow, and M. E. Peskin, Phys. Rev. D **49**, 3209 (1994).
[54] I. F. Ginzburg, G. L. Kotkin, V. G. Serbo, and V. I. Telnov, Nucl. Instrum. Methods A **205**, 47 (1983).
[55] I. F. Ginzburg, G. L. Kotkin, V. G. Serbo, and V. I. Telnov, Nucl. Instrum. Methods A **219**, 5 (1984).
[56] V. I. Telnov, Nucl. Instrum. Methods A **294**, 72 (1990).
[57] CELLO Collaboration, H. J. Behrend *et al.*, Z. Phys. C **51**, 365 (1991).
[58] PLUTO Collaboration, C. Berger *et al.*, Z. Phys. C **29**, 499 (1985).

[59] PLUTO Collaboration, C. Berger *et al.*, Z. Phys. C **33**, 351 (1987).
[60] DELPHI Collaboration, P. Abreu *et al.*, Z. Phys. C **62**, 357 (1994).
[61] ALEPH Collaboration, D. Buskulic *et al.*, Phys. Lett. B **313**, 509 (1993).
[62] TOPAZ Collaboration, H. Hayashii *et al.*, Phys. Lett. B **314**, 149 (1993).
[63] AMY Collaboration, B. J. Kim *et al.*, Phys. Lett. B **325**, 248 (1994).
[64] D. Morgan, M. R. Pennington, and M. R. Whalley, J. Phys. G **20**, A1 (1994).
[65] T. Kleinwort and G. Kramer, Phys. Lett. B **370**, 141 (1996).
[66] M. Drees and R. M. Godbole, Report No. MADPH-95-898, BU-TH-95/2, hep-ph/9508221 (unpublished).
[67] M. Drees and R. M. Godbole, Z. Phys. C **59**, 591 (1993).
[68] R. Brinkmann, presentation at the Linear Collider workshop, Gran Sasso, Italy (unpublished).
[69] G. A. Schuler and T. Sjöstrand, Report No. CERN-TH/96-119, LU-TP 96-13, hep-ph/9605240 (unpublished).
[70] PLUTO Collaboration, M. Feindt *et al.*, talk given at 7th International Workshop on photon-photon interactions, Paris (unpublished).
[71] TPC/2γ Collaboration, H. Aihara *et al.*, Phys. Rev. D **41**, 2667 (1990).
[72] PLUTO Collaboration, C. Berger *et al.*, Phys. Lett. **149B**, 421 (1984).
[73] D. Bintinger *et al.*, Phys. Rev. Lett. **54**, 763 (1985).
[74] T. Kafka *et al.*, Phys. Rev. D **16**, 1261 (1977).
[75] A. E. Brenner *et al.*, Phys. Rev. D **26**, 1497 (1982).
[76] EHS-RCBC Collaboration, M. Aguilar-Benitez *et al.*, Z. Phys. C **50**, 405 (1991).
[77] EHS-RCBC Collaboration, J. L. Bailly *et al.*, Z. Phys. C **35**, 309 (1987).